Surface photogalvanic effect in Weyl semimetals

J. F. Steiner, A. V. Andreev, and M. Breitkreiz

¹Dahlem Center for Complex Quantum Systems and Fachbereich Physik, Freie Universität Berlin, 14195 Berlin, Germany

²Skolkovo Institute of Science and Technology, Moscow 143026, Russia

³Department of Physics, University of Washington, Seattle, Washington 98195, USA

⁴L. D. Landau Institute for Theoretical Physics, Moscow 119334, Russia



(Received 25 October 2021; revised 19 March 2022; accepted 22 March 2022; published 8 April 2022)

The photogalvanic effect—a rectified current induced by light irradiation—requires the intrinsic symmetry of the medium to be sufficiently low, which strongly limits candidate materials for this effect. In this paper we explore how in Weyl semimetals the photogalvanic effect can be enabled and controlled by design of the material surface. Specifically, we provide a theory of ballistic linear and circular photogalvanic current in a Weyl semimetal spatially confined to a slab under general and variable surface boundary conditions. The results are applicable to Weyl semimetals with an arbitrary number of Weyl nodes at radiation frequencies small compared to the energy of nonlinear terms in the dispersion at the Fermi level. The confinement-induced response is tightly linked to the configuration of Fermi-arc surface states, specifically the Fermi-arc connectivity and direction of emanation from the Weyl nodes, thus inheriting the same directionality and sensitivity to boundary conditions. As a result, the photogalvanic response of the system becomes much richer than that of an infinite system, and may be tuned via surface manipulations.

DOI: 10.1103/PhysRevResearch.4.023021

I. INTRODUCTION

In the past decade, Weyl semimetals (WSMs) have attracted great attention, from theoretical prediction [1] to experimental realization [2–5]. Of particular interest are the peculiar transport phenomena [6,7] due to the presence of Weyl fermions, the associated chiral anomaly [8–10], and topological Fermi-arc surface states [1,11]. For instance, WSMs are considered a promising platform for optoelectronic applications [12,13] because chirality and the topologically protected linear dispersion of Weyl fermions generally tend to enable and enhance the response to incident light [14]. The relevant light frequencies lie typically in the mid- and far-infrared region, bounded from below by the typically small but finite chemical potential at the Weyl nodes and from above by the onsetting nonlinear corrections to the Weyl dispersion.

Most discussed is the photogalvanic effect (PGE) in noncentrosymmetric WSMs—a *dc* current response to light irradiation [15–24]. Generally, the photogalvanic current density may be expanded as [25,26]

$$\boldsymbol{J} = \sum_{i,j=x,y,z} \boldsymbol{\Gamma}_{ij} \mathcal{E}_i \mathcal{E}_j^*, \tag{1}$$

where \mathcal{E} is the polarization vector of the light field and Γ is the photogalvanic response tensor. One distinguishes between a ballistic current, induced by asymmetric in momentum pho-

Published by the American Physical Society under the terms of the Creative Commons Attribution 4.0 International license. Further distribution of this work must maintain attribution to the author(s) and the published article's title, journal citation, and DOI.

togeneration (or injection following the terminology of [27]), which is proportional to the relaxation time and dominates in clean samples, and the shift current, which is finite even in the absence of relaxation processes. Notably, in noncentrosymmetric WSMs a quantized photogeneration induced by circularly polarized light was predicted and observed [28,29]. WSMs that in addition to inversion also break time-reversal symmetry may further exhibit a ballistic response to linearly polarized light, which may be giant [17,24,30–33].

Besides the bulk PGE that can be understood in terms of infinite-system models, the PGE has been explored at the surfaces of metals [34–36] and topological insulators [37–40], in which case the surface-normal component of Γ (but not that of \mathcal{E}) vanishes. In the field of WSMs, recently there was evidence from experiments and first principles calculations that Fermi arc states might play an important role in the photogalvanic response [41,42], a contribution that was neglected in previous theories. In particular, Chang *et al.* [42] have shown that the contribution of surface states to the PGE due to excitations between the surface states of the same surface are possible in chiral crystals due to high Chern numbers and a nonlinear dispersion of those surface states.

The mere presence of surface states, however, does not capture the full peculiarity of a WSM. Importantly, the *two*-dimensional Fermi-arc surface states, constituting in some sense the reaction of a pair of chiral Weyl fermions to confinement, are tightly glued to the *three*-dimensional Weyl fermions [43], as illustrated in Fig. 1(a). This *connectivity* distinguishes Fermi arcs from surface states of metals and topological insulators and was shown to give rise to a number intriguing, counter-intuitive linear-response effects [44–54]. Understanding its role also for the photogalvanic response is highly desirable. The theoretical challenge to capture the

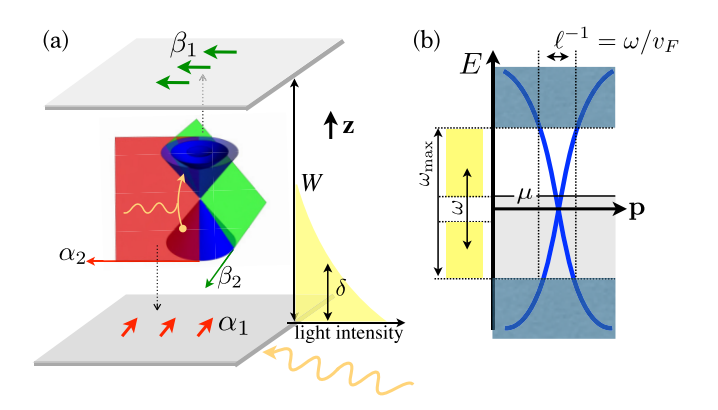


FIG. 1. (a) Dispersion (energy vs in-plane momenta) of Weyl fermions confined to a slab of thickness W. The plot shows bulk states (blue) and surface states of bottom surface (red) and top surface (green). The surface states are tightly *glued* to the bulk Weyl cone and emanate in the direction α_2 ($-\beta_2$) for bottom (top) surface. The figure also shows the directions of Fermi-arc motion (α_1 and β_1), as well as the photon penetration depth δ . (b) Low-energy band structure at the Weyl node. The Fermi energy μ and the energy range of the linear-dispersion regime ω_{max} determine the range of considered photon frequencies $2\mu < \omega < \omega_{\text{max}}$.

effect of the connectivity is the requirement to go beyond an effective surface theory and consider a full three-dimensional, yet spatially confined, model.

In this paper we present a theory of ballistic photogalvanic response of Weyl fermions spatially confined in one direction with general boundary conditions, relevant for Weylsemimetal slabs with an arbitrary configuration of Weyl nodes and arbitrary orientations of Fermi arcs at the bottom and top surfaces, which need not be the same.

Specifically, the orientation of the bottom (top) Fermi arc is defined by the direction of its velocity α_1 (β_1) or the perpendicular direction at which the arc emanates from the Weyl node α_2 (- β_2), see Fig. 1(a). We show that this symmetry-breaking directionality gives rise to a vastly richer response behavior compared to an unconfined WSM. In particular, the confinement enables the otherwise vanishing linear and circular PGE in centrosymmetric WSMs. Furthermore, the response is crucially determined by the orientations of the Fermi arcs. The latter may be adjusted by choosing different surface terminations [55,56] or surface doping [57]. In principle, this allows control over the photogalvanic response by modification of the surface only.

To focus on Weyl physics, we consider a photon frequency range for which excitations can take place only close to Weyl nodes where the bulk and arc dispersions are linear, see Fig. 1(b). The total response is then the sum of the responses of individual Weyl nodes. Further, we focus on the semimetallic regime, in which the Fermi level μ is close to the Weyl node and smaller than the photon energy, such that Pauli blocking as well as screening may be neglected. In this regime, intrasurface (arc-arc) excitations are forbidden [58], but bulk-bulk excitations as well as arc-bulk excitations exist.

Most strikingly, for a centrosymmetric WSM confined to a slab, the photogalvanic response is fully determined by the Fermi-arc orientation. Considering the current density in Eq. (1) as the current density averaged over the slab width, the response tensor can be decomposed into a confinement-independent bulk-bulk contribution Γ^{bb} and confinement-induced contributions, which in turn consist of bulk-bulk $\delta\Gamma^{bb}$ as well as arc-bulk Γ^{ab} parts,

$$\Gamma = \Gamma^{bb} + \delta \Gamma^{bb} + \Gamma^{ab}.$$
 (2)

For a centrosymmetric WSM, Γ^{bb} vanishes according to general symmetry considerations [25]. The response is thus given by

$$\mathbf{\Gamma}^{\text{centrosymm.}} = \delta \mathbf{\Gamma}^{\text{bb}} + \mathbf{\Gamma}^{\text{ab}},\tag{3}$$

where both contributions are fully determined by the Fermiarc orientations since the orientation of the arcs and modification of the bulk-state wave functions are both defined by the boundary conditions. Moreover, a centrosymmetric WSM necessarily breaks time-reversal symmetry, which implies that $\Gamma^{\text{centrosymm.}}$ will include a ballistic response to linearly polarized light of the type discussed in [31]. This is directly relevant to magnetic WSMs, such as $\text{Co}_3\text{Sn}_2\text{S}_2$ [59], RhSi [29], and GdPtBi [60]. Table I summarizes which types of photogalvanic response are possible in unconfined and confined WSMs, depending on the mechanism and the presence of time-reversal and inversion symmetry.

Finally, the confinement-induced PGE is categorized depending on the slab thickness. For a sufficiently thick slab or sufficiently high frequency the light field does not penetrate the whole slab. This is the case when the penetration depth δ , which for photon energies $\hbar\omega\sim 1$ meV to 1 eV lies in the range 1 μ m to 1 mm, is much smaller than the slab thickness W. For light incident at the bottom surface, see Fig. 1(a), the top surface no longer contributes to the response. This changes the symmetry of the response tensor. We refer to this limit as

TABLE I. Allowed types of photogalvanic response in WSMs, bCPGE, sCPGE, bLPGE, and sLPGE, distinguished by light polarization, circular (CPGE) and linear (LPGE), and origin (b for bulk) and (s for surface). Setups are categorized by mechanism (ballistic/shift current) and presence/absence of time-reversal and inversion symmetry of the WSM material. Terms in parentheses give subdominant response in clean systems. Italic text marks contributions first discussed in this work. In the presence of inversion symmetry, the bulk photogalvanic response vanishes and only surface contributions remain. In this case, the response is fully determined by the directionality of the Fermi arcs. In particular, there is a surface induced ballistic LPGE enabled by broken time-reversal symmetry.

Symmetry	Time reversal (broken inversion)	Inversion (broken time reversal)	Neither	
Ballistic current (injection) Shift current	bCPGE, <i>sCPGE</i> bLPGE, sLPGE	sCPGE, sLPGE (sCPGE, sLPGE)	bCPGE, bLPGE, sCPGE, sLPGE (bCPGE, bLPGE, sCPGE, sLPGE)	

the *thick slab*. In the opposite limit, referred to as the *thin slab*, $\delta \gg W$, both surfaces contribute. Technically, the two limits require substantially different calculations, we will thus mostly consider the thick- and thin-slab regimes separately, using different analytical and numerical techniques.

This article is organized as follows. In Sec. II we introduce the model of a WSM in the slab geometry for which we perform our calculations. We also briefly discuss the decay of light waves in WSMs. Finally, we present the semiclassical formulas for the photogalvanic current that we employ. In Sec. III we classify the different contributions to the photogalvanic response tensor and estimate their magnitude. Further, we comment on the irrelevance of finite light momentum. In Sec. IV we discuss the symmetry constraints on the response tensor. Finally, in Sec. V we present analytical results for the different contributions to the response tensor for a single Weyl cone in the different regimes. We further present a lattice simulation in the thin limit, which confirms the analytical results. At the end of this section we apply our results to WSMs with several Weyl cones by considering a centrosymmetric WSM with two nodes. We conclude in Sec. VI. Technical details are delegated to the Appendices.

II. MODEL

A. Weyl semimetal

We consider a WSM slab with a set of Weyl nodes, which are close to the Fermi level. We also assume that the projections of the Weyl points to the surface Brillouin zone are well separated. Since we consider the response to excitations occurring close to the Weyl nodes only, it suffices to consider the response of a single Weyl node, from which the response of a WSM with several Weyl nodes will follow by combining the single-Weyl-node response tensors, transformed according to the specific Weyl-node arrangement.

In order to evaluate the matrix elements relevant for the photogalvanic response tensors we seek explicit expressions for the wave-functions in the slab geometry (see Appendix A for a detailed derivation). To this end, we model a single Weyl fermion confined to 0 < z < W with the Hamiltonian (we set $\hbar = 1$)

$$H = \chi v \mathbf{p} \cdot \mathbf{\sigma},\tag{4}$$

where p is the momentum (with $p_z = -i\partial_z$), σ the spin, $\chi = \pm$ the chirality, and v the velocity. For better transparency of the following calculations we here assume isotropic velocity of the Weyl fermion; in Appendix B we generalize the results to an anisotropic Weyl node, which leads to a simple transformation of the response tensor. In the absence of a tilt, the Weyl Hamiltonian Eq. (4) commutes with the operator $\mathcal{T} = i\sigma_y K$, where K is complex conjugation. By analogy with relativistic theory we refer to this intranode symmetry as time reversal (TR) symmetry. Note that it does not correspond to the time reversal operation acting on the whole crystal, as this connects different Weyl nodes. Thus the intranode TR symmetry allows to constrain the response due to a single Weyl node only. A WSM with several Weyl nodes at generic points in momentum space clearly does not need to satisfy TR symmetry.

Using translation invariance parallel to the surface we seek energy eigenstates in the form of plane waves in the xy

plane with the continuous in-plane momenta $p_{\parallel}=(p_x,p_y)\equiv p_{\parallel}(\cos\phi,\sin\phi)$. Their dependence on z is given by the solutions to the Weyl equation $H\psi(z)=E\psi(z)$, which may be written as

$$\psi(z) \propto \exp\{i\mathcal{P}_z z\}\psi(0)$$

$$\propto (p_z \cos(p_z z) + i \sin(p_z z)\mathcal{P}_z)\psi(0), \tag{5}$$

where $p_z = \sqrt{E^2 - p_{\parallel}^2}$ and the generalized momentum operator reads

$$\mathcal{P}_z = \left(ip_y, -ip_x, \frac{\chi E}{v}\right) \cdot \boldsymbol{\sigma}. \tag{6}$$

The discrete energy eigenvalues of the slab (at fixed p_{\parallel}) are to be determined by boundary conditions. A generic boundary condition on the wave function is a vanishing current j_z across the boundaries. Since $j_z \propto \partial_{p_z} H \propto \sigma_z$ this corresponds to $\psi^{\dagger} \sigma_z \psi = 0$. Accounting for the possibility of differing boundary conditions for the bottom and top surfaces, a general boundary condition thus reads

$$\psi(0) \propto \begin{pmatrix} 1 \\ e^{i\alpha} \end{pmatrix}, \qquad \psi(W) \propto \begin{pmatrix} 1 \\ e^{i\beta} \end{pmatrix},$$
 (7)

parametrized by two independent angles α and β . Surface inhomogeneities would correspond to a spatial dependence of α and β . Here we assume translation invariance at the surface (up to a relaxation mean free path that will be introduced perturbatively below) and thus consider α and β to be constant.

The boundary conditions lead to the equation

$$\sin \frac{\beta - \alpha}{2} = \frac{\tan(p_z W)}{p_z} \left[p_{\parallel} \cos \left(\phi - \frac{\beta + \alpha}{2} \right) \right]$$

$$\mp \chi p \cos \frac{\beta - \alpha}{2}, \qquad (8)$$

which determines the quantized eigenvalues p_z . Solutions with real p_z correspond to bulk states, imaginary solutions correspond to surface "arc" states. For details and explicit expressions of the arc and bulk states see Appendix A. Note that α and β define the velocity of the Fermi arcs localized at the bottom (b) and top (t) surfaces,

$$\mathbf{v}_{\text{arc}}^{\text{b}} = \chi v \boldsymbol{\alpha}_{1}, \quad \mathbf{v}_{\text{arc}}^{\text{t}} = \chi v \boldsymbol{\beta}_{1}.$$
 (9)

as well as the direction at which they emanate from the Weyl node, given by the constraint

$$\mathbf{p} \cdot \mathbf{\alpha}_2 \equiv \kappa_b > 0, \quad \mathbf{p} \cdot (-\mathbf{\beta}_2) \equiv \kappa_t > 0,$$
 (10)

for bottom and top arc, respectively, where we defined the vectors

$$\alpha_1 = \begin{pmatrix} \cos \alpha \\ \sin \alpha \\ 0 \end{pmatrix}, \quad \alpha_2 = \begin{pmatrix} -\sin \alpha \\ \cos \alpha \\ 0 \end{pmatrix}, \quad (11a)$$

$$\boldsymbol{\beta}_1 = \begin{pmatrix} \cos \beta \\ \sin \beta \\ 0 \end{pmatrix}, \quad \boldsymbol{\beta}_2 = \begin{pmatrix} -\sin \beta \\ \cos \beta \\ 0 \end{pmatrix}.$$
 (11b)

The quantities κ_t and κ_b introduced in Eq. (10) have the meaning of inverse decay lengths of the evanescent wave

functions of arc states at the top and bottom surfaces respectively.

In order to analyze symmetries in the presence of the boundary conditions, it proves helpful to define an equivalent multilayer setup, which reproduces the same spectrum and wave functions as the boundary conditions Eq. (7). Note that this is a fictitious system only introduced to assist in understanding the response of a single Weyl node. The equivalent multilayer setup is defined by the Hamiltonian

$$H_{\chi m} = \chi v \boldsymbol{p} \cdot \boldsymbol{\sigma} + \begin{cases} -\chi m \, \boldsymbol{\sigma} \cdot \boldsymbol{\alpha}_2 & z < 0 \\ 0 & 0 < z < W, \\ \chi m \, \boldsymbol{\sigma} \cdot \boldsymbol{\beta}_2 & z > W \end{cases}$$
(12)

with $m \to \infty$ [61,62]. Under TR the multilayer Hamiltonian transforms like

$$\mathcal{T}^{-1}H_{\chi m}\mathcal{T} = H_{\chi - m}.\tag{13}$$

The mass terms of the boundary conditions thus behave like TR-breaking magnetizations in the directions $-\chi \alpha_2$ and $\chi \beta_2$ at the two boundaries. Note that this does not imply TR-breaking of the WSM with several Weyl nodes.

Furthermore, note that the directions of the boundary spinors can be additionally controlled by TR-preserving boundary potentials [57]. One can easily check that adding a boundary potential $\delta H_b = \delta(z)\mu_0 + \delta(z - W)\mu_W$ to the Hamiltonian (12), rotates the boundary spinors like $\alpha \rightarrow \alpha +$ $\chi 2\mu_0$ and $\beta \to \beta - \chi 2\mu_W$. Boundary potentials are typically disregarded in minimal models of Weyl-semimetal slabs, which corresponds to straight arcs connecting the Weyl cones, i.e., $\beta = \alpha + \pi$. Here we instead consider the general case that the Fermi arcs can emanate in any direction, considering the boundary spinors (7) to be given by two independent variables α and β . The resulting curvature of Fermi arcs, which is necessary to connect pairs of Weyl nodes and is often observed in experiments, is irrelevant in the close vicinity of the Weyl nodes to which the optical transitions that we consider are bound. The directionality introduced by the boundary conditions will crucially determine the direction of the response. It is therefore convenient to define the coordinate axes along the emergent high-symmetry directions. Those depend on whether current is induced at a single surface (thick-slab case) or in the whole slab (thin-slab case). Figure 2 illustrates the geometry and the high-symmetry axes in these two cases.

B. Electromagnetic waves in Weyl semimetals

For frequencies $\omega \gtrsim \mu$ the conductivity in WSMs is given by [6,63]

$$\sigma(\omega) = N \frac{e^2}{24\pi\epsilon_{\infty} v} |\omega| = N \frac{\xi}{24\pi} |\omega|, \tag{14}$$

Here, N is the total number of Weyl nodes in the system, $\epsilon_{\infty} \sim 10$ is the permittivity due to inert bands and we let $e^2 \to e^2/\epsilon_{\infty}$ to account for screening. Finally, we defined the dimensionless coupling constant

$$\xi = \frac{e^2}{\epsilon_{\infty} v} = \frac{1}{137} \times \frac{c}{v} \times \frac{1}{\epsilon_{\infty}} \sim 0.1.$$
 (15)

Note that $\mathcal{N} = N\xi/6$ takes values between 1/30 and 1 in a WSM, depending on the number of nodes. The imaginary

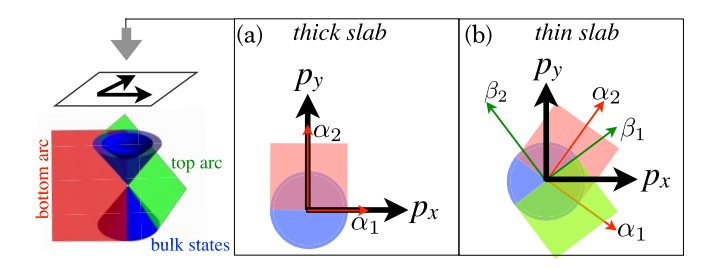


FIG. 2. Top view on the slab dispersion (left, see also Fig. 1) showing the choice of coordinate axes p_x and p_y to lie along high-symmetry directions in (a) the thick-slab ($W \gg \delta$) and (b) the thin-slab case ($W \ll \delta$). The slab dispersion features bulk states (blue), surface states of bottom (red) and top (green) surfaces. In (a) only the bottom surface matters since the light penetrating over the depth δ at the bottom surface does not reach the top arc.

part of σ has only weak frequency dependence and has been absorbed into ϵ_{∞} . The frequency dependent permittivity then reads

$$\epsilon(\omega) = \epsilon_{\infty} \left[1 + \frac{4\pi i}{\omega} \sigma(\omega) \right] = \epsilon_{\infty} \left[1 + i \frac{N\xi}{6} \operatorname{sign}(\omega) \right].$$
 (16)

We consider light entering the WSM at the z = 0 surface. The field *inside* the WSM has the form,

$$E(\mathbf{r}, t) \propto \exp i(\mathbf{k} \cdot \mathbf{r} - \omega t) \exp -z/\delta,$$
 (17)

where k is the momentum inside the medium and δ is the penetration depth. In terms of the vacuum wave number $k_v = \omega/c$ and to leading order in \mathcal{N} , they are given by

$$|\mathbf{k}| = \sqrt{\epsilon_{\infty}} k_v (1 + \mathcal{N}^2)^{1/4} \cos \frac{\arctan \mathcal{N}}{2} \simeq \sqrt{\epsilon_{\infty}} k_v,$$
 (18a)

$$\frac{1}{\delta} = \sqrt{\epsilon_{\infty}} k_v (1 + \mathcal{N}^2)^{1/4} \sin \frac{\arctan \mathcal{N}}{2} \simeq \frac{\sqrt{\epsilon_{\infty}} \mathcal{N}}{2} k_v.$$
 (18b)

With the above estimate of \mathcal{N} , depending on the number of Weyl nodes, we thus obtain $k\delta \sim 1...10$.

C. Photogalvanic response tensor

We consider the response of the Weyl slab to the weak external oscillating electric field

$$\boldsymbol{E}(\boldsymbol{r},t) = \left[\boldsymbol{\mathcal{E}}e^{i\boldsymbol{k}\cdot\boldsymbol{r}-i\omega t} + \text{c.c.}\right]e^{-z/\delta}.$$
 (19)

In the temporal gauge $E = -\partial_t A$, the perturbation to the Hamiltonian reads

$$\delta H = \mathbf{j} \cdot \mathbf{A}(\mathbf{r}, t) = i \chi e \ell \mathcal{E} \cdot \sigma e^{-i\omega t} e^{i\mathbf{k} \cdot \mathbf{r} - z/\delta} + \text{H.c.}, \quad (20)$$

where $\mathbf{j} = -e\chi v\sigma$ is the current operator and $\ell = v/\omega$ is the smallest length scale of our model. In the following we will use dimensionless length and momenta, denoted with a tilde:

$$\tilde{r} = \frac{r}{\ell}, \quad \tilde{p} = p \ell,$$
 (21)

in units of ℓ and ℓ^{-1} , respectively.

The ballistic PGE can be described within the framework of the Boltzmann kinetic equation by balancing asymmetric photogeneration and impurity-induced relaxation. Using the standard perturbation theory and relaxation-time approximation, one can express the photogalvanic response in terms of the momentum relaxation time τ in the form [17,27]

$$\Gamma_{ij} = \frac{8\pi \eta \tau}{\tilde{W}} \int d^2 \tilde{p}_{\parallel} \sum_{q_z p_z} \left(\frac{\boldsymbol{v}_{p+}}{v} - \frac{\boldsymbol{v}_{q-}}{v} \right) \times \delta \left(1 - \frac{E_p}{\omega} - \frac{E_q}{\omega} \right) \left(\boldsymbol{M}_{pq} \otimes \boldsymbol{M}_{pq}^* \right)_{ij}$$
(22)

where \otimes denotes the dyadic product, $\boldsymbol{p}=(\boldsymbol{p}_{\parallel},p_z)$, $\boldsymbol{q}=(\boldsymbol{p}_{\parallel}-\boldsymbol{k}_{\parallel},q_z)$, $d^2\tilde{p}_{\parallel}=\ell^2d\boldsymbol{p}_{\parallel}$, and we introduced the matrix elements

$$\mathbf{M}_{pq} = \langle +, \mathbf{p} | \mathbf{\sigma} e^{i\mathbf{k} \cdot \mathbf{r} - z/\delta} | -, \mathbf{q} \rangle, \tag{23}$$

and the constant (restoring \hbar , which is set to one)

$$\eta = \frac{e^3}{16\pi^2\hbar^2}.\tag{24}$$

Note that $4\pi \eta$ is the quantum of the CPGE trace and may be assumed large compared to ordinary PGE magnitudes [28]. These expressions hold for both bulk-bulk and and arc-bulk excitations. To avoid overcounting of states, for bulk states the sum runs only over $p_z>0$ while for arc states it runs over $\Im p_z>0$. Note that $\Gamma_z=0$ as $v_z=0$ for all states due to the boundary conditions.

The relaxation-time approximation of Eq. (22) neglects energy and momentum dependencies, as well as forward-scattering corrections. Especially in the interplay of surface and bulk states, those can lead to potentially interesting quantitative refinements [54] of the results, which is left for future work. We also neglect interaction effects, which are known to modify the PGE quantitatively [64].

Note that the three 3×3 matrices Γ are hermitian. According to standard terminology, the imaginary antisymmetric part is associated with the circular PGE, which is present only if the incident light is elliptically polarized (the inverse implication is not true: elliptically polarized light can give rise to photogalvanic response stemming from the real symmetric part). The real symmetric part is referred to as the linear photogalvanic response, which exists even for linearly polarized radiation.

III. CLASSIFICATION AND ESTIMATE OF RESPONSE CONTRIBUTIONS

There are three relevant length scales in the problem [65], the v/c-weighted light wavelength $\ell = v/\omega$, the light penetration depth δ , and the slab thickness W, whereby the weighted light wavelength is always much smaller than the penetration depth, $\ell/\delta \sim v/c \sim 10^{-2}$. The width W is considered in two limits, the *thick-slab case* $W \gg \delta$ and the *thin-slab case* $\delta \gg W$. In the thick-slab case the light completely decays inside the slab and only a single slab surface is excited. In the thin-slab case the light penetrates nearly homogeneously the whole slab such that both surfaces are equally excited. In this limit, for simplicity of analytical calculations we introduce a lower bound for the width, $W \gg \ell$, so that energy quantization of slab modes is small compared to the light frequency. The ultrathin case $W \sim \ell$ will be considered numerically on a lattice model.

TABLE II. Scaling of the confinement-independent contribution $\Gamma^{\rm bb}$ and the confinement-induced contributions $\delta \Gamma^{\rm bb}$, $\Gamma^{\rm ab}$ with relevant length scales of the system (W,ℓ,δ) in the cases of a thin and thick slab.

	Thick slab $W \gg \delta$	Thin slab $\delta \gg W$	
$oldsymbol{\Gamma}^{\mathrm{bb}}$	$rac{\delta}{W}=rac{ar{\delta}}{ar{W}}$	1	
$\delta \Gamma^{bb}, \Gamma^{ab}$	$\frac{\ell}{W} = \frac{1}{\tilde{W}}$	$rac{\ell}{W}=rac{1}{ ilde{W}}$	

Before coming to the detailed calculation, it is useful to classify the response contributions according to their dependencies on the relevant length scales (ℓ, δ, W) , separating confinement-independent from confinement-induced contributions and distinguishing contributions due to arc-bulk and bulk-bulk excitations as given in (2). The result is summarized in Table II and is explained in the following.

To estimate the magnitudes of contributions it suffices to disregard the spin degree of freedom and consider the bulk wave functions to be of the form $|q\rangle = \exp(iq_zz)/\sqrt{W}$ and that of arc states of the form $|q\rangle = \exp(-z/\ell)/\sqrt{l}$. In the latter, the inverse decay length κ , given in (10), has been approximated by the typical inverse distance from the Weyl node in the active region of excitations, which is set by $\ell^{-1} \equiv \omega/v$. Neglecting the in-plane light momentum k (will be justified below), the matrix elements (23) for the thick-slab case can be estimated as

$$|\mathbf{M}|^2 \sim \begin{cases} \left(\frac{\delta}{W}\right)^2 \frac{1}{1 + [(q_z - p_z)\delta]^2} & \text{bulk-bulk} \\ \frac{\ell}{W} \frac{1}{1 + (q_z \ell)^2} & \text{arc-bulk.} \end{cases}$$
(25)

The momentum separation of modes is 1/W, hence the number of modes within the active range around the node is W/ℓ . The summation over p_z and q_z thus gives

$$\sum_{n,a} |\mathbf{M}|^2 \sim \begin{cases} \frac{\delta}{\ell} & \text{bulk-bulk} \\ 1 & \text{arc-bulk} \end{cases}$$
 (26)

and the magnitude of the response tensor will thus scale like

$$\Gamma^{\rm bb} \sim \frac{\delta}{W}, \qquad \Gamma^{\rm ab} \sim \frac{\ell}{W},$$
(27)

for bulk-bulk and arc-bulk excitations, respectively.

Since $\delta \gg \ell$, bulk-bulk excitations will give the dominant current contribution, while the confinement-induced correction due to arc-bulk excitations give the finite-size correction with the small parameter ℓ/δ . Importantly, there are also contributions due to bulk-bulk excitations possible that scale like those from arc-bulk excitations,

$$\delta\Gamma^{\rm bb} \sim \Gamma^{\rm ab}$$
. (28)

To see this, note that the contribution $\Gamma^{\rm bb}$ stems from approximating the peaked behavior of the bulk-bulk matrix elements in (25) at $q_z = p_z$ by a delta function, the correction to setting $q_z = p_z$ is of the order ℓ/δ because the peak width is $1/\delta$ and the effective integration range $1/\ell$. Hence the leading correction scales like the arc-bulk contribution, and needs to be taken into account.

Upon changing the scales from the thick-slab case, $W \gg \delta$, to the thin-slab case, $\delta \gg W$, the scaling of the contribution of

arc-bulk excitations does not change because the localization length of most arc states κ^{-1} , given in (10), is set by ℓ and hence much smaller than both W and δ .

For bulk-bulk excitations, the matrix elements are now the overlaps of wave functions over the whole slab width,

$$|\mathbf{M}|^2 \sim \frac{1 - \cos[(q_m - q_n)W]}{[(q_m - q_n)W]^2}.$$
 (29)

Summation over p_z and q_z gives $\sum_{p_zq_z}|\pmb{M}|^2\sim \tilde{W}$ and the magnitude of the current thus scales like

$$\Gamma^{\rm bb} \sim 1,$$
 (30)

missing the factor δ/W as compared to the limit $W \gg \delta$ given in (27), since transitions are now produced across the full width of the slab.

As before, the matrix elements are peaked at $q_m = q_n$; the correction $\delta \Gamma^{bb}$ to the $q_m = q_n$ contribution Γ^{bb} is of order l/W because the peak width is now 1/W, while the integration range is still $1/\ell$. Thus $\delta \Gamma^{bb} \sim \Gamma^{ab}$ remains valid also in the thin-slab limit. This concludes the explanation of the scaling summarized in Table II.

A. Irrelevance of the light momentum

The momentum transfer due to a finite light momentum has the magnitude $k \sim \omega/c$. The small parameter of corrections due to this momentum shift is k/p, where $p \sim 1/\ell = \omega/v$ is the typical momentum of excited states, hence $k/p \sim v/c \sim$ 0.01. Comparing the smallness of corrections to the response, those due to a finite k are irrelevant for the thin-slab case but potentially relevant in the case of a thick slab, where they are on the same order as the finite-size corrections, cf. Table II. It turns out, however, that corrections to leading order in $k/p \sim v/c$ vanish also for the thick-slab case, which we show explicitly for our slab model in Appendix E. An easier way to find the same result is to realize that considering the correction due to a finite k/p, one can neglect the finite-size corrections, which would give terms that are quadratic in the small parameter. Neglecting finite-size corrections, the result should thus coincide with that of an infinite system. In particular, the directionality introduced by the confinement becomes irrelevant. It is straightforward to verify that for a bulk Weyl cone the first-order k/p corrections vanish.

For the response tensor in Eq. (22) this means that k can be set to zero, the matrix elements become

$$\mathbf{M}_{pq} = \langle +, \mathbf{p} | \sigma e^{-z/\delta} | -, \mathbf{q} \rangle, \tag{31}$$

and the momenta have the same parallel component, $p = (p_{\parallel}, p_z), q = (p_{\parallel}, q_z).$

Finally, we comment on the spatial structure of the confinement induced response current. While our calculation considers only the spatial average of the current, we expect the spatial profile of the photogalvanic current to be uniform. This can be understood as follows. The total number of electrons in the surface Fermi arc states is unaffected by the perturbation, as just as many electrons are excited to positive energy Fermi arc states from the bulk as electrons are excited from negative energy Fermi arc states to the bulk. Close to the Weyl point all Fermi arc states have the same velocity. Hence, the net velocity due to Fermi arcs is unchanged. The non-equilibrium

current stems from the asymmetric population of bulk states and hence is expected to be spatially uniform.

IV. SYMMETRY CONSTRAINTS

As the last preliminary consideration before coming to the explicit results, we now consider symmetry constraints on the response tensor. Considering the transition matrix elements (31) we realize that since the band index \pm enters the wave functions in the form $\pm \chi$, which can be explicitly seen in Appendix A, Eq. (A9), we obtain the relation

$$M_{pq}^*\big|_{\chi} = M_{qp}\big|_{-\chi}.\tag{32}$$

Using this and that other terms in the response expression, Eq. (22), are symmetric in $p \leftrightarrow q$, we conclude that

$$(\mathbf{\Gamma} \pm \mathbf{\Gamma}^T)_{\mathbf{y}} = \pm (\mathbf{\Gamma} \pm \mathbf{\Gamma}^T)_{-\mathbf{y}},$$
 (33)

showing that the (anti)symmetric part of the response tensor is even (odd) in the chirality χ . Moreover, generally the (anti)symmetric part of the response tensor is odd (even) under TR [25], which, according to the transformation behavior (13) is given by $m \to -m$ (in the fictitious multilayer system) and thus

$$(\mathbf{\Gamma} \pm \mathbf{\Gamma}^T)_m = \mp (\mathbf{\Gamma} \pm \mathbf{\Gamma}^T)_{-m}.$$
 (34)

For the thick-slab case, only the bottom surface is involved and $m \to -m$ corresponds to inversion of $\alpha_2 \equiv \hat{y}$, i.e., mirror reflection R_y with respect to the xz plane. Taking into account also symmetry with respect to R_x , the response tensor assumes the form

$$\mathbf{\Gamma}^{\text{thick}} = \hat{\mathbf{x}} \begin{pmatrix} 0 & \Gamma_{xxy} & 0 \\ \Gamma_{xxy} & 0 & \Gamma_{xyz} \\ 0 & -\Gamma_{xyz} & 0 \end{pmatrix} + \hat{\mathbf{y}} \begin{pmatrix} \Gamma_{yxx} & 0 & -\Gamma_{yzx} \\ 0 & \Gamma_{yyy} & 0 \\ \Gamma_{yzx} & 0 & \Gamma_{yzz} \end{pmatrix}. \tag{35}$$

For the thin-slab case, both surfaces are involved and combinations of two reflections leave the Hamiltonian invariant or time reversed. In the thin-slab basis [Fig. 2(c)] we obtain

$$R_{\nu}R_{\tau}H_{\nu m}R_{\tau}R_{\nu} = H_{\nu m}, \tag{36a}$$

$$R_x R_y H_{\gamma m} R_y R_x = H_{\gamma - m}. \tag{36b}$$

The resulting transformation behavior of the response tensor dictates the form

$$\mathbf{\Gamma}^{\text{thin}} = \hat{\boldsymbol{x}} \begin{pmatrix} \Gamma_{xxx} & 0 & 0 \\ 0 & \Gamma_{xyy} & \Gamma_{xyz} \\ 0 & -\Gamma_{xyz} & \Gamma_{xzz} \end{pmatrix} + \hat{\boldsymbol{y}} \begin{pmatrix} 0 & \Gamma_{yxy} & -\Gamma_{yzx} \\ \Gamma_{yxy} & 0 & 0 \\ \Gamma_{yzx} & 0 & 0 \end{pmatrix}.$$
(37)

A more detailed derivation of the tensor forms is given in Appendix C.

V. RESULTS

A. PGE due to arc-bulk excitations

Arc-bulk excitations give rise to a current that is "automatically" a finite-size effect. Other finite-size corrections are negligible, which can be used to simplify the expression for the response tensor in Eq. (22); we can disregard the quantization of modes and replace the sums by integrals. The integration over z in the matrix elements of Eq. (31) may be extended to infinity since the decay of surface modes at most momenta is on the order of $\ell \ll \delta$, W, in both the thick-slab and thin-slab limits. Moreover we can neglect confinement-induced corrections of bulk states. A straightfor-

$$\frac{\mathbf{\Gamma}^{\text{ab,thin}}}{4\pi \, \eta \tau / \tilde{W}} = \hat{\mathbf{x}} \begin{pmatrix} \ln 2 \, \sin^3 \Delta & 0 & 0 \\ 0 & \ln 2 \, \sin \Delta \, \cos^2 \Delta & i \frac{8}{3} \chi \, \cos^2 \Delta \\ 0 & -i \frac{8}{3} \chi \, \cos^2 \Delta & \ln 2 \, \sin \Delta \end{pmatrix} + \hat{\mathbf{y}} \, \sin \Delta \begin{pmatrix} 0 & \ln 2 \, \cos^2 \Delta & -i \frac{8}{3} \chi \, \sin \Delta \\ \ln 2 \, \cos^2 \Delta & 0 & 0 \\ i \frac{8}{3} \chi \, \sin \Delta & 0 & 0 \end{pmatrix}, \quad (39)$$

where we defined

$$\Delta = \frac{\beta - \alpha}{2}.$$

To understand this result, it suffices to understand the current production due to arc-bulk excitations at a single (bottom) surface, illustrated in Fig. 3. First we note that arc-bulk excitations vanish for the polarization component x because such a photon does not act on the spinor of the arc (which is an eigenspinor of σ_x) and thus cannot induce a transition to the orthogonal bulk state. This is circumvented when the linear polarization points in the other directions, y and z. The induced velocity due to arc-bulk excitations sum up to a total velocity pointing in the \hat{y} direction, see Fig. 3(c), which explains the second term of (38).

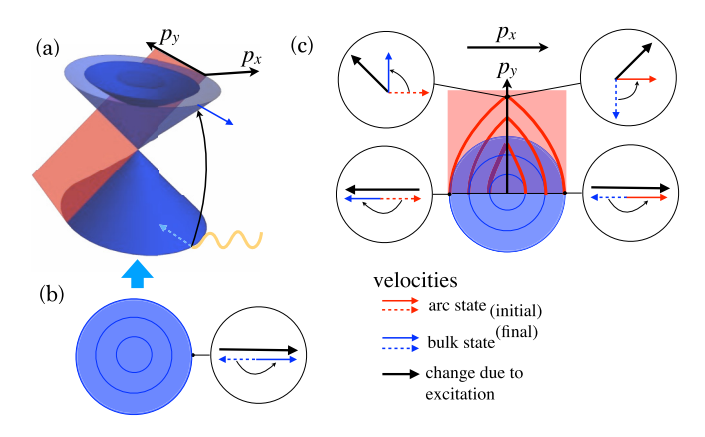


FIG. 3. (a) Dispersion of Weyl fermions confined to a slab as function of in-plane momenta in the thick slab basis. Bulk states are colored blue and the Fermi-arc surface states red (only the bottom surface is shown). Velocities of initial (dashed arrow) and final state (solid arrow) of a photoexcitation are indicated. (b) Top view on bulk states in (a) showing the velocity change due to a bulk-bulk excitation. (c) Same as (b) but with indicated velocity change from arc-bulk excitations. Red contours indicate those states of the surface arc states that satisfy the energy-conservation constraint for arc-bulk excitations $\omega = \chi v p_x \pm v p$.

ward calculation (see Appendix D for details) then gives

$$\mathbf{\Gamma}_{ij}^{\text{ab,thick}} = \frac{2\pi \eta \tau}{\tilde{W}} \left[i \chi \frac{8}{3} \varepsilon_{xij} \hat{\mathbf{x}} + \ln(2) \, \delta_{ij} (1 - \delta_{xi}) \hat{\mathbf{y}} \right]$$
(38)

for the bottom arc in the thick-slab basis $\hat{x} = \alpha_1$, $\hat{y} = \alpha_2$ [Fig. 2(b)]. The antisymmetric part is expressed using the Levi-Civita symbol ε_{ijk} . This is the only arc-bulk contribution in the thick-slab case.

In the thin-slab case we add the contribution of the top arc, which is equivalent to the bottom arc up to the changed directions, $\alpha_1 \to \beta_1$, $\alpha_2 \to -\beta_2$, see Fig. 2. Adding both contributions after appropriate rotation into the thin-slab basis [Fig. 2(c)] we obtain

Circular y + iz polarization instead acts like a ladder operator on the σ_x eigenspinor and thus enhances the amplitude of spin-flip excitations where the spin is increased (at positive p_x in Fig. 3) and suppresses those where the spin is lowered (at negative p_x in Fig. 3), and vice versa for the opposite polarization handedness, y - iz, or chirality χ of the Weyl fermions. As is clear from Fig. 3, this asymmetry can produce velocity in the x direction, which sign depends on the polarization handedness and the chirality. This explains the first term of Eq. (38).

B. PGE due to bulk-bulk excitations

In contrast to the arc-bulk excitations, the contribution of excitations within the bulk bands (from the valence bulk band to the conduction bulk band) strongly differ for the thin- and thick-slab cases. We thus consider the two cases separately.

1. Thick slab limit $W \gg \delta$

In this limit the light-induced excitations are produced at a single (bottom) surface in the finite strip of width δ . For the confinement-independent contribution Γ^{bb} we neglect all finite-size effects and obtain (see Appendix E 1 for details)

$$\Gamma_{ij}^{\text{bb,thick}} = i\chi \frac{2\pi \eta \tau}{3} \frac{\delta}{W} \left(\varepsilon_{xij} \hat{\boldsymbol{x}} + \varepsilon_{yij} \hat{\boldsymbol{y}} \right). \tag{40}$$

Apart from the absence of current in the direction perpendicular to the boundary and the factor δ/W , this expression is identical to the circular PGE found in the infinite system model [17], which here has been rederived using slab eigenstates. It is manifestly independent of the orientation of the Fermi arc. The prefactor δ/W correctly reflects the fact that excitations occur in the fraction of the penetration depth of the full sample width.

The leading corrections in the thick-slab limit are of a higher order in ℓ/δ , see Table II. They stem from the z integration in the matrix elements (31), where we can still take the limit $W \to \infty$ but keep the finite light penetration depth. Other finite-size corrections are controlled by the small parameter ℓ/W and can thus be neglected. Expansion to leading

order in ℓ/δ and numerical evaluation of the integral gives (see Appendix E 1 for details)

$$\frac{\delta \mathbf{\Gamma}^{\text{bb,thick}}}{\eta \tau / \tilde{W}} \simeq \hat{\mathbf{x}} \begin{pmatrix} 0 & 4.2 & 0 \\ 4.2 & 0 & -16.8 i \chi \\ 0 & 16.8 i \chi & 0 \end{pmatrix} + \hat{\mathbf{y}} \begin{pmatrix} -4.2 & 0 & 9.9 i \chi \\ 0 & -4.2 & 0 \\ -9.9 i \chi & 0 & -8.4 \end{pmatrix}, \tag{41}$$

written in the thick-slab basis, $\alpha_1 = \hat{x}$, $\alpha_2 = \hat{y}$. We estimate that these expressions are accurate to below 0.5%. Corrections to the circular PGE (antisymmetric part of the tensor) are in the same tensor components as the leading terms, as they should according to the symmetry constraints. The corrections are of opposite sign as the leading contribution because the tendency of the boundary to align the initial and final spinor suppresses the transition amplitude (circular PGE needs spinflip processes). A difference between x and y components is a manifestation of the boundary-condition-broken symmetry between the x and y directions.

The response to linearly polarized light (symmetric part of the tensor) is something that is not found for an infinite-system Weyl cone in the absence of tilt. This follows from the fact that a single unconfined tiltless Weyl node is intranode TR symmetric and hence there is no linear PGE. The vanishing of the linear PGE in such a system is due to cancellation of the linearly-polarized-light-induced current from states at opposite momenta parallel to the polarization [17]. While the symmetry considerations have already shown that linear PGE contributions are possible in the presence of a boundary, (which breaks intranode TR symmetry) it is peculiar that these contributions stem not only from arc-bulk but also from bulk-bulk excitations. To understand how the boundary breaks the symmetry between opposite momenta of bulk states, we consider the bulk-state spinor as a function of z, explicitly given in Eq. (A9). At z = 0 the boundary condition forces the spinors at all momenta to coincide with $\psi(0) \propto (1, \exp[i\alpha])$. Going away from the boundary, the spinors rotate in the in-plane basis: At small z the spinor can be written as (1, $\exp[i\Phi(z)]$), with $\Phi(z) = -2 \arctan[(\pm \chi p - p_x)z]$. Since $p > |p_x|$, the rotation handedness is the same for all momenta and is set only by the chirality and the band (\pm) . The spin averaged over the whole slab width coincides with the spin of an infinite system—parallel or antiparallel to the momentum, depending on the band and chirality. As illustrated in Fig. 4, the angle between the spinor at z = 0 and the averaged spinor, measured in the direction of rotation, thus always differs by π for opposite momenta, which provides the crucial symmetry breaking and enables the response to linearly polarized radia-

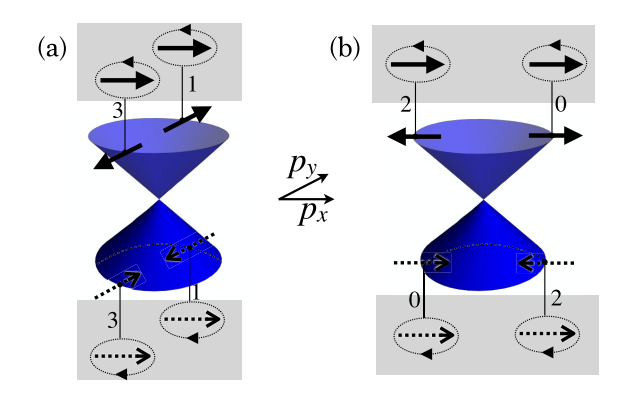


FIG. 4. Characterization of bulk Weyl spinors in a semi-infinite spatial geometry. Spinors at the boundary are shown as arrows in the gray areas. They point in the x direction for all states. Going away from the boundary the spinors rotate so that the average spin, indicated as arrows at the cones, are like in an infinite system pointing parallel or antiparallel to the momentum, depending on the band and chirality (here positive). The numbers characterize the angle between the boundary and the average spinor (in units of $\pi/2$), which differ by π for opposite momenta. [(a), (b)] Spinors at momenta perpendicular and parallel to the boundary spinor, respectively.

tion. Moreover, as can be seen from Eq. (A9) and in Fig. 4(b), the x (i.e., α_1) component of the spinor is invariant under simultaneous band change and $p \rightarrow -p$, which explains the vanishing diagonal components for the response in the x direction.

2. Thin slab $\delta \gg W \gg \ell$

The confinement-independent contribution Γ^{bb} is obtained similarly to the thick-slab case by neglecting all finite-size corrections. The only difference is that the integration over z now extends over the whole slab width instead of δ . The result,

$$\mathbf{\Gamma}_{ij}^{\text{bb,thin}} = i\chi \frac{4\pi \eta \tau}{3} \left(\varepsilon_{xij} \hat{\mathbf{x}} + \varepsilon_{yij} \hat{\mathbf{y}} \right), \tag{42}$$

is, up to the missing factor $\delta/2W$, identical to the thick-slab case and, up to the vanishing current normal to the slab, identical to the known infinite-system result, as it should.

For the confinement-induced contributions we collect finite-size corrections of the type ℓ/W . They stem from the quantization of q_z and p_z as well as from corrections to the wave functions and the velocity of bulk states. We solve the problem numerically via discretizing the polar angle ϕ , and finding q_z , p_z pairs satisfying the energy conservation and Eq. (8) using standard numerical tools (see Appendix E 2 for details), yielding

$$\frac{\delta \mathbf{\Gamma}^{\text{bb,thin}}}{\eta \tau / \tilde{W}} \simeq \hat{\mathbf{x}} \begin{pmatrix}
-14.1 \sin \Delta + 4.7 \sin 3\Delta & 0 & 0 \\
0 & -21.5 \sin \Delta - 4.7 \sin 3\Delta & -i\chi (26.7 + 6.9 \cos 2\Delta) \\
0 & i\chi (26.7 + 6.9 \cos 2\Delta) & -23.0 \sin \Delta
\end{pmatrix} \\
+ \hat{\mathbf{y}} \begin{pmatrix}
0 & 3.7 \sin \Delta - 4.7 \sin 3\Delta & i\chi (26.5 - 6.9 \cos 2\Delta) \\
-i\chi (26.5 - 6.9 \cos 2\Delta) & 0 & 0
\end{pmatrix}, \tag{43}$$

where we defined

$$\Delta \equiv \frac{\beta - \alpha}{2}.\tag{44}$$

The numerical coefficients are accurate to the first decimal. Together with Eqs. (38) and (41), Eq. (43) represents the central quantitative result of this work. Because of scale invariance of the Weyl Hamiltonian, these results are generic for any Weyl semimetal with untilted Weyl cones, up to straightforward directional rescaling in case of anisotropic velocity, as discussed in Appendix B.

C. Discussion of confinement induced contributions and comparison to lattice simulation

The arc-bulk contribution Γ^{ab} and the confinement-induced bulk-bulk contribution $\delta\Gamma^{bb}$ are intimately linked: They are of the same order of magnitude and they always occur in combination. Therefore, only the sum $\delta\Gamma^{bb}+\Gamma^{ab}$ is experimentally relevant.

In the thick-slab limit, the confinement-induced response tensor is

$$\frac{\delta \mathbf{\Gamma}^{\text{bb,thick}} + \mathbf{\Gamma}^{\text{ab,thick}}}{\eta \tau / \tilde{W}}$$

$$\simeq \hat{\mathbf{x}} \begin{pmatrix} 0 & 4.2 & 0 \\ 4.2 & 0 & 0 \\ 0 & 0 & 0 \end{pmatrix} + \hat{\mathbf{y}} \begin{pmatrix} -4.2 & 0 & 9.9i\chi \\ 0 & 0.2 & 0 \\ -9.9i\chi & 0 & -4.0 \end{pmatrix}.$$
(45)

Note that since $\Gamma^{bb, thick}_{xyz}$ and $\Gamma^{ab, thick}_{xyz}$ cancel (within numerical accuracy), circularly polarized light may produce a sizable current only parallel to the Fermi arc $(\alpha_2 = \hat{y})$, whereas linearly polarized light may produce currents perpendicular to the Fermi arc as well.

The thin-slab limit result is plotted in Fig. 5 as a function of Δ . For $\beta = \alpha$ ($\Delta = 0$), the linear PGE vanishes because the second surface restores the symmetry between opposite momenta: With regard to the corresponding discussion for the

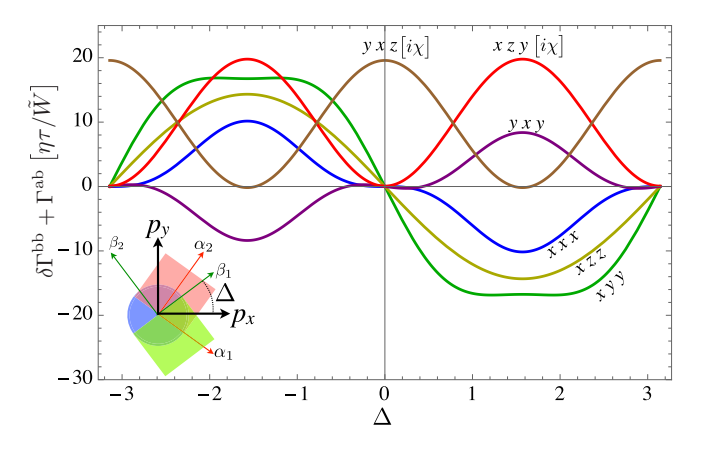


FIG. 5. Confinement-induced response tensor $\delta \Gamma^{bb,thin}_{ijk} + \Gamma^{ab,thin}_{ijk}$ as a function of Δ . Only nonzero components are shown, labeled with ijk, the circular-PGE components have an additional prefactor $i\chi$ as indicated.

thick-slab limit, the sense of rotation of spinors away from the z=W boundary is opposite to z=0 since z runs "backwards" there. For $\beta=\pm\pi+\alpha$ ($\Delta=\pm\pi/2$) the symmetric part of the response tensor is approximately maximized, while the weight of circular response is simply shifted from one component to the other. The Fermi arc orientations thus change the nature of the response completely.

More generally, one can understand that the (anti)symmetric part of the tensor, i.e., the linear (circular) PGE, must be odd (even) in Δ . In terms of Δ , the TR-breaking directions in (12) are given by $\alpha_2 = (-\sin \Delta, \cos \Delta)$ and $\beta_2 = (\sin \Delta, \cos \Delta)$. The transformation $\Delta \to -\Delta$ combined with the reflection R_x and $\chi \to -\chi$ leaves the Hamiltonian invariant. From the corresponding transformation of the tensor follows that components of the symmetric part are odd while components of the anti-symmetric part are even in Δ , as seen in Fig. 5.

While for clarity of the analysis we considered the thin-slab case assuming $W\gg\ell$, it is possible to relax this constraint and consider ultrathin slabs with $W\sim\ell$ resorting to numerical techniques. In this regime also transitions between arc states of the different surfaces become important. Here, we used a one-dimensional lattice realization of a single Weyl node (discretizing the z direction while keeping r_{\parallel} continuous) to numerically evaluate the photogalvanic response tensor in Eq. (22). Details can be found in Appendix F. The results are shown in Fig. 6, demonstrating that our semi-analytical results can be reproduced in a lattice setting, and that the qualitative behavior, such as sign and magnitude of the confinement induced contributions, extends down to $W\sim\ell$. For $W\lesssim2\ell$, the finite-size gap of modes becomes larger than the photon energy and the response vanishes.

D. Centrosymmetric Weyl semimetal

Our results for a single Weyl node allow to infer on the response of a WSM with several nodes by adding the contributions of each node. Probably the most interesting case is that of centrosymmetric WSMs, for which the confinementindependent bulk-bulk contributions Γ^{bb} cancel and only the confinement-induced contributions, $\delta\Gamma^{bb}$ and Γ^{ab} , survive. A minimal model of a centrosymmetric bulk WSM consists of a single pair of Weyl nodes with opposite chirality. Considering the multilayer Hamiltonian $H_{\chi m}$ in (12) as the Hamiltonian describing one of the Weyl nodes, for the Hamiltonian describing the second Weyl node of opposite chirality we take $H_{-\gamma-m}$. In this case the Fermi arcs emanate in opposite directions, which happens when the Weyl nodes are connected in a straight line. However, we have seen in Sec. II that an additional boundary potential $\delta H_b = \delta(z)\mu_0 + \delta(z - W)\mu_W$ rotates the spinors by $\alpha \to \alpha + \chi 2\mu_0$ and $\beta \to \beta - \chi 2\mu_W$. The generic situation is thus that there is a finite angle φ characterizing the deviation from an antiparallel alignment, as shown in the inset of Fig. 7(a). Note that between the nodes, the Fermi arcs thus must be curved, as is typically seen in experiments; the curvature itself plays however no role for our results since excitations occur only close to the Weyl nodes.

The total response $\Gamma^{\text{WSM}}_{abc}$ is obtained from the single-cone result $\Gamma_{ijk}(\chi, m)$ (now explicitly denoting the χ, m dependent

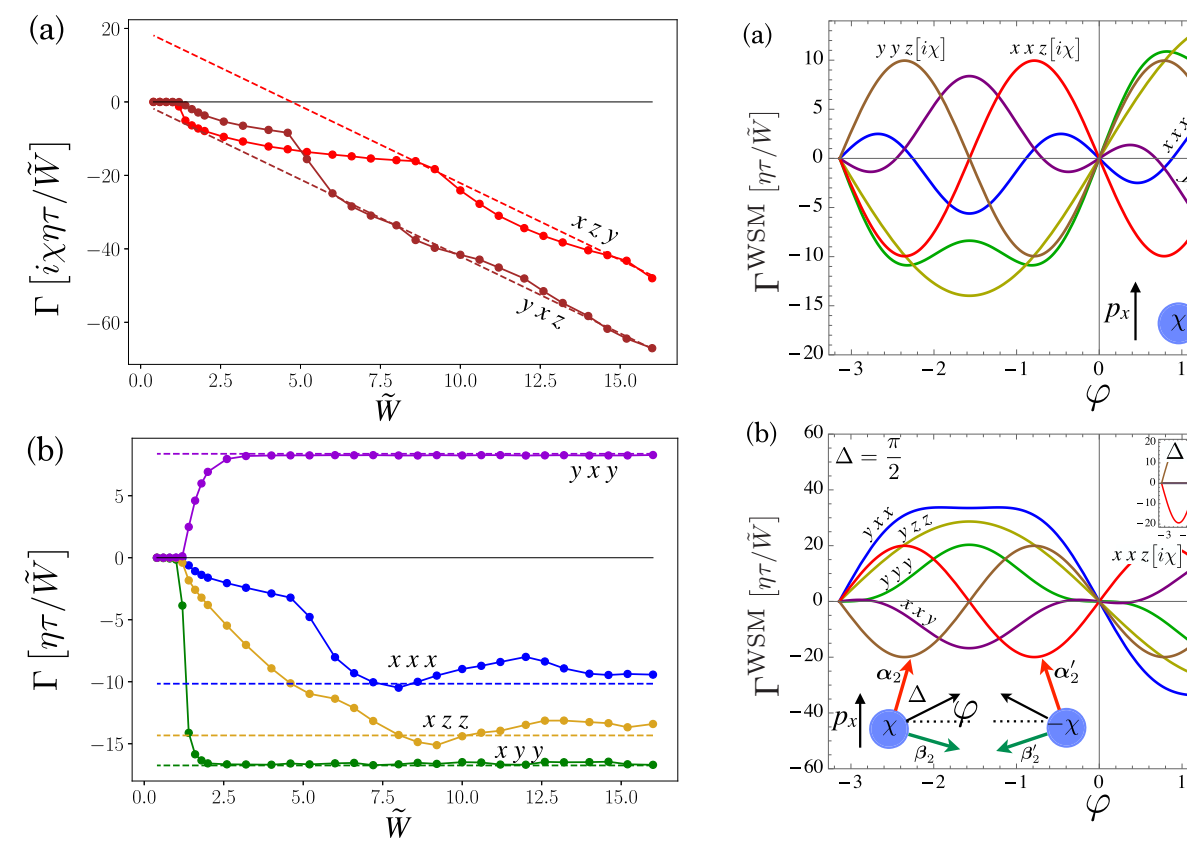


FIG. 6. (a) Circular and (b) linear response tensor components in the ultrathin limit $\tilde{W}=W/\ell\sim 1$ at $\Delta=\pi/2$. The data points correspond to the photogalvanic response tensor Eq. (22) numerically evaluated for a lattice realization of a single Weyl point (see Appendix F for details). The dashed lines correspond to the semi-analytical results $\Gamma=\Gamma^{bb}+\delta\Gamma^{bb}+\Gamma^{ab}$ in the limit $\tilde{W}\gg 1$. For $\tilde{W}\lesssim 2$, the lattice response vanishes as the frequency drops below the finite size gap. For $\tilde{W}\gtrsim 2$, the response converges towards the semi-analytical $\tilde{W}\gg 1$ results.

dence),

$$\Gamma_{abc}^{WSM} = R(\varphi)_{ai} R(\varphi)_{bj} R(\varphi)_{ck} \Gamma_{ijk}(\chi, m) + R(-\varphi)_{ai} R(-\varphi)_{bj} R(-\varphi)_{ck} \Gamma_{ijk}(-\chi, -m), \quad (46)$$

where $R(\varphi)$ is the spatial rotation matrix for a rotation around z by φ . The results are plotted in Fig. 7. From the transformation behavior of the response tensor discussed in Sec. IV (symmetric part odd in m and even in χ , antisymmetric part odd in χ and even in m), the response of the two Weyl nodes cancel each other at $\varphi=0$. This means that in the thick-slab case the response vanishes when the Fermi arcs of the illuminated surface emanate from the Weyl nodes in exactly opposite directions. In the thin-slab case, the same applies but the emanation direction is replaced by the bisector of the top-and bottom-surface Fermi arcs.

For $\phi = \pi/2$ the directions just discussed (emanation direction for thick slab and bisector direction for thin slab) are parallel. This is equivalent to taking the contributions of the two Weyl nodes at the same m (instead of m and -m), while χ are still opposite. Since the (anti)symmetric part is even (odd) in χ , the antisymmetric parts cancel also here but

FIG. 7. Response-tensor components for a centrosymmetric WSM in (a) the thick- and (b) the thin-slab case, as a function the angle φ . As shown in the lower insets, ϕ sets the deviation from antiparallel alignment of (a) the direction of bottom-surface Fermi arcs; and (b) the directions of bisectors of bottom- and top-surface Fermi arcs. In the thin-slab case (b) the angle between top and bottom arcs is chosen as $\Delta = \pi/2$; the inset in the right top shows the result for $\Delta = 0$, for which the linear PGE vanishes.

the symmetric parts add up to twice the value of a single cone. This can be seen by comparison of Fig. 7(b) with the single-cone results shown in Fig. 5 for the thin-slab case and Fig. 7(a) with $\Gamma^{\text{ab,thick}} + \delta \Gamma^{\text{bb,thick}}$ from Eqs. (38) and (41) for the thick-slab case. (Note that the coordinate system is now rotated by $\pi/2$, i.e., $y \to x$ and $x \to -y$, compared to the single-cone case).

VI. CONCLUSION

In conclusion, we have explored the PGE of a WSM spatially confined to a slab geometry. Symmetry breaking on the surfaces via the orientation of the Fermi arcs enables circular and linear photogalvanic response currents, which would otherwise not be possible, in particular, in centrosymmetric WSMs.

The magnitude of the confinement-enabled PGE inherits the topology-enhancement of unconfined Weyl fermions, based on the topologically protected band touchings [28,30]. However, while in infinite systems those band touchings include only the chiral pairs of Weyl nodes, a confined system features topological surface states, which are tightly glued to the Weyl nodes.

The ratio of confinement-induced contributions to bulk contributions scales in case of a thin slab like $(v/c) \times (\lambda/W)$ and for the thick slab like v/c, where λ is the light wavelength, W the slab thickness, and $v/c \approx 0.01$ the node- versus light-velocity. Considering the upper and lower bounds of λ set by the finite Fermi level and the band width of typical WSM materials, the confinement-induced PGE is on the order of bulk PGE for widths of order $W \sim 0.1 \dots 1 \, \mu \text{m}$. Surface-controlled PGE is thus found in such thin slabs even for noncentrosymmetric WSMs, which makes the experimental realization of thin WSM slabs or even stacks of those especially interesting.

One of the most remarkable properties of the confinementinduced PGE is that it is controlled by surface boundary conditions. We explicitly discussed the effect of a surface potential, which rotates the direction of Fermi arcs. Another interesting possibility, known from experiments, are layered WSMs for which the different surface terminations can not only change the directionality of Fermi arcs but even lead to different connectivities to the Weyl nodes [55,56]. This Fermi-arc geometry is observable, e.g., via angle-resolved photoemission spectroscopy [3-5]; our paper links this geometry with the photogalvanic response. In principle, a confinement-related photogalvanic response may exist also in regular metals due to Tamm surface states. However, such a response does not share the remarkable features of the confinement-induced PGE in WSMs. The difference is due to topology: While in a regular metal, the surface state wavefunctions depend on microscopic details, in a WSM the Fermi arc wave functions are uniquely determined by the Fermi arc directionality. This fact enables the sensitivity to boundary conditions and hence the control of the confinement-induced PGE in WSM. Moreover, a confinement-related PGE in a regular metal would lack the aforementioned enhancement due to the band touchings in a WSM and should hence be much smaller than the effect discussed in this paper.

With regard to the remarkable recent progress in device microstructuring [48,66–69], our paper might thus play an important role in identifying Weyl physics and shaping the photogalvanic response by designing the material surface.

Note added. Recently, we became aware of a recent article [70] considering the PGE of a finite system using a minimal centrosymmetric lattice model that features two Weyl nodes. This article focuses on Fermi energies far away from the Weyl nodes where the PGE is governed by nonlinear terms of the dispersion, while in the semimetallic regime, which is the focus of our paper, the response of their model vanishes as it, in terms of our model, considers only the specific $\varphi=0$ case of Sec. V D. This trivial case is the only place of overlap of our papers.

ACKNOWLEDGMENTS

We benefited from a discussion with Haim Beidenkopf. J.F.S. gratefully acknowledges financial support by QuantERA project *Topoquant*, as well as by the Deutsche Forschungsgemeinschaft (DFG, German Research Foundation) through Priority Program 1666 and CRC 910. M.B. was funded by Grant No. 18688556 of the DFG. The work of A.A.

was supported by the National Science Foundation Grant No. MRSEC DMR-1719797.

APPENDIX A: CONFINED WEYL FERMION WAVE FUNCTIONS

In this Appendix we derive the explicit form of the eigenfunctions of Eq. (4) in the slab geometry 0 < z < W. Writing the momentum operator p_z in the spatial basis, $p_z = -i\partial_z$ the Weyl equation $H\psi(z) = E\psi(z)$ can be written as

$$-i\partial_z \psi(z) = \mathcal{P}_z \psi(z), \tag{A1}$$

where the generalized momentum \mathcal{P}_z was defined in Eq. (6). The Weyl equation is formally solved by Eq. (5). Defining an orthonormal basis for our model of zero out-of-plane current states,

$$|\alpha_{\pm}\rangle = \frac{1}{\sqrt{2}} \begin{pmatrix} 1 \\ \pm e^{i\alpha} \end{pmatrix}, \quad |\beta_{\pm}\rangle = \frac{1}{\sqrt{2}} \begin{pmatrix} 1 \\ \pm e^{i\beta} \end{pmatrix}, \quad (A2)$$

the generic boundary conditions at the two surfaces can be written as

$$\psi(0) \propto |\alpha_{+}\rangle, \quad \psi(W) \propto |\beta_{+}\rangle.$$
 (A3)

From the boundary conditions, the quantized eigenvalues p_z are the solutions of

$$0 = \sin \frac{\alpha - \beta}{2} + \frac{\tan(p_z W)}{p_z} \left[p_x \mp \chi p \cos \frac{\alpha - \beta}{2} \right], \quad (A4)$$

where p_x is in the basis of Fig. 2(c). Solutions with real p_z correspond to bulk states, imaginary solutions correspond to surface "arc" states, which we will now discuss in more detail.

1. Arc states

For an imaginary p_z , normalizable wave functions are found that are localized at the bottom (b) and top (t) surfaces,

$$\psi_{\rm arc}^{\rm b}(z) = \sqrt{2\boldsymbol{p}\cdot\boldsymbol{\alpha}_2} \; e^{-\boldsymbol{p}\cdot\boldsymbol{\alpha}_2 z} |\alpha_+\rangle = \langle z|{\rm arc,b},\boldsymbol{p}_\parallel\rangle, \tag{A5a}$$

$$\psi_{\rm arc}^{\rm t}(z) = \sqrt{-2\boldsymbol{p}\cdot\boldsymbol{\beta}_2} \, e^{\boldsymbol{p}\cdot\boldsymbol{\beta}_2(W-z)} |\beta_+\rangle = \langle z|{\rm arc,t},\boldsymbol{p}_\parallel\rangle. \ \ ({\rm A5b})$$

(These expressions assume $W|\mathbf{x}_2 \cdot \mathbf{p}| \gg 1$ for $x \in \{\alpha, \beta\}$.) From the criterion of normalizability, the momenta of Fermi arcs are bound to

$$\boldsymbol{p} \cdot \boldsymbol{\alpha}_2 > 0, \quad \boldsymbol{p} \cdot \boldsymbol{\beta}_2 < 0.$$
 (A6)

The dispersion relations read

$$E_{\text{arc}}^{\text{b}} = \chi v \boldsymbol{p} \cdot \boldsymbol{\alpha}_{1}, \quad E_{\text{arc}}^{\text{t}} = \chi v \boldsymbol{p} \cdot \boldsymbol{\beta}_{1},$$
 (A7)

and hence the velocity expectation values are

$$\mathbf{v}_{\text{arc}}^{\text{b}} = \chi v \boldsymbol{\alpha}_{1}, \quad \mathbf{v}_{\text{arc}}^{\text{t}} = \chi v \boldsymbol{\beta}_{1}.$$
 (A8)

The directions α_i and β_i are thus the directions in which the Fermi arcs emanate from the Weyl node (i = 1) and the directions of their motion (i = 2), both up to the sign, as indicated in Fig. 2.

2. Bulk states

For a real p_z , from (5) the normalized wave functions of the conduction (+) and valence band (-) read

$$\psi_{p\pm}(z) = \frac{1}{\sqrt{WN_{p\pm}}} \{ [p_z \cos p_z z - \boldsymbol{\alpha}_2 \cdot \boldsymbol{p} \sin p_z z] | \boldsymbol{\alpha}_+ \rangle$$

$$+ i [\pm \chi \, p - \boldsymbol{\alpha}_1 \cdot \boldsymbol{p}] \sin p_z z | \boldsymbol{\alpha}_- \rangle \}$$

$$= \langle z | \text{bulk}, \pm, \boldsymbol{p} \rangle,$$
(A9)

where the normalization factor, isolating the finite-size correction $\sim 1/W$, is given by

$$N_{p\pm} = p(p \mp \chi \boldsymbol{\alpha}_{1} \cdot \boldsymbol{p}) + \delta N_{p\pm}, \qquad (A10a)$$

$$\delta N_{p\pm} = -\frac{\sin(W p_{z})}{W p_{z}} [(p_{\parallel}^{2} \mp \chi p \, \boldsymbol{\alpha}_{1} \cdot \boldsymbol{p}) \cos(W p_{z}) + p_{z} \boldsymbol{\alpha}_{2} \cdot \boldsymbol{p} \sin(W p_{z})]. \qquad (A10b)$$

The velocity expectation values read

$$\boldsymbol{v}_{p\pm} = \pm v \frac{\boldsymbol{p}_{\parallel}}{p} + \delta \boldsymbol{v}_{p\pm}, \tag{A11a}$$

$$\delta \mathbf{v}_{p\pm} = \frac{\partial E_{p\pm}}{\partial p_z} \frac{dp_z}{d\mathbf{p}} = \pm v \frac{p_z}{p} \frac{dp_z}{d\mathbf{p}}, \quad (A11b)$$

where we again isolated the finite-size correction $\delta \pmb{v}_{\pmb{p}\pm} \sim 1/W$, which stems from the weak \pmb{p}_{\parallel} dependence of the quantized p_z , as implicitly given in (8). Note that $v_z=0$ due to the boundary conditions for all states.

APPENDIX B: ANISOTROPIC WEYL NODE

Here we generalize our calculations to Weyl fermions with anisotropic velocity. We consider the Hamiltonian

$$h'(\mathbf{p}) = v_{ij}\sigma_i p_j \equiv \chi v \mathbf{p}' \cdot \boldsymbol{\sigma} = h(\mathbf{p}'),$$
 (B1)

where $v_{ij} = v_{ji}$ and we defined $p'_i = \tilde{v}_{ij}p_j$ in terms of

$$\tilde{v}_{ij} = \chi \frac{v_{ij}}{v}, \ v > 0. \tag{B2}$$

The chirality of the anisotropic Weyl node is $\chi = \text{sign}(\det v)$. Undashed symbols refer to the isotropic case discussed in the main text. The current operator is

$$j_i' = -ev_{ij}\sigma_j = \tilde{v}_{ij}j_j. \tag{B3}$$

To avoid complications in the boundary condition we specify to

$$v = \operatorname{diag}(v_{\parallel}, v_{\tau}), \tag{B4}$$

where v_{\parallel} is a 2 x 2 matrix acting only on components parallel to the boundary. Furthermore, we set $v=|v_z|$. With this we may again employ the boundary conditions of Eq. (7). Then, the arc and bulk wave functions may be obtained by simply replacing $p \rightarrow p'$ in Eqs. (A5a), (A5b), and (A9). Similarly, the velocities can be expressed in terms of the isotropic expressions via

$$\left(\mathbf{v}_{p,n}'\right)_{i} = \frac{dE_{p,n}'}{dp_{i}} = \frac{\partial p_{i}'}{\partial p_{i}} \frac{dE_{p',n}}{dp_{i}'} = \tilde{v}_{ij} (\mathbf{v}_{p',n})_{j}.$$
(B5)

Altogether, the response tensor of the anisotropic Weyl node is related to the isotropic node via [c.f. Eq. (22)]

$$\Gamma'_{ijk} = \frac{8\pi \eta \tau}{W} \int d^2 p_{\parallel} \sum_{q,p} \left(\frac{v'_{p+}}{v} - \frac{v'_{q-}}{v} \right)_i \delta \left(1 - \frac{E'_p}{\omega} - \frac{E'_q}{\omega} \right) \left[\mathbf{M}'_{pq} \otimes (\mathbf{M}'_{pq})^* \right]_{jk}$$
(B6a)

$$= \frac{\tilde{v}_{il}\tilde{v}_{jm}\tilde{v}_{kn}}{|\det \tilde{v}|} \frac{8\pi \eta \tau}{W} \int d^2 p'_{\parallel} \sum_{q',p'} \left(\frac{\boldsymbol{v}_{p'+}}{v} - \frac{\boldsymbol{v}_{q'-}}{v} \right)_{l} \delta \left(1 - \frac{E_{p'}}{\omega} - \frac{E_{q'}}{\omega} \right) \left[\boldsymbol{M}_{p'q'} \otimes \boldsymbol{M}_{p'q'}^{*} \right]_{mn}$$
(B6b)

$$=\frac{\tilde{v}_{il}\tilde{v}_{jm}\tilde{v}_{kn}}{|\det \tilde{v}|}\Gamma_{lmn},\tag{B6c}$$

where the determinant stems from the change of variables p_{\parallel} to p'_{\parallel} (using $|\det \tilde{v}_{\parallel}| = |\det \tilde{v}|$ due to our choice of v).

APPENDIX C: SYMMETRY CONSIDERATIONS

1. Thick slab

We work in the basis of the thick slab $\alpha_1 = \hat{x}$, $\alpha_2 = \hat{y}$. The heterostructure Hamiltonian Eq. (12) of the semi-infinite system under consideration can be written as

$$H_{\chi m} = \chi v \mathbf{p} \cdot \mathbf{\sigma} + \begin{cases} -\chi m \sigma_y & z < 0 \\ 0 & z > 0 \end{cases}$$
 (C1)

where the vacuum at z < 0 is modeled by a large mass term with $m \to \infty$, which acts like a magnetization in breaking the intra-node TR symmetry, as discussed in the main text. We consider spatial mirror-plane reflections R_i , i = x, y, z, with i = x corresponding to reflection with respect to the yz plane, etc. A single reflection reverses the component of the

momentum and the current that is normal to the mirror plane and the components of the spin that are parallel to the mirror plane. The action of the reflections on the Hamiltonian thus read

$$R_x H_{\chi m} R_x = H_{-\chi m}, \quad R_y H_{\chi m} R_y = H_{-\chi - m}.$$
 (C2)

In words, reflection R_x reverses the chirality and reflection R_y reverses the chirality and the magnetization.

From this we can infer on the transformation behavior of the response tensor. First, note that the (anti)symmetric part of the response tensor Γ^s (Γ^a) is generally odd (even) under TR [25]—the (anti)symmetric part is thus odd (even) under $m \to -m$. Second, in Sec. IV we have shown that the (anti)symmetric part of the response tensor is even (odd) under $\chi \to -\chi$. Taking also into account the transformation

of the current under reflections, we obtain for the symmetric part,

$$R_x \Gamma_x^s R_x = -\Gamma_x^s, \tag{C3a}$$

$$R_x \Gamma_v^s R_x = \Gamma_v^s, \tag{C3b}$$

$$R_{\nu}\Gamma_{\nu}^{s}R_{\nu} = -\Gamma_{\nu}^{s}, \tag{C3c}$$

$$R_{\nu}\Gamma_{\nu}^{s}R_{\nu} = \Gamma_{\nu}^{s}, \tag{C3d}$$

while the antisymmetric part satisfies

$$R_x \Gamma_x^{as} R_x = \Gamma_x^{as},$$
 (C4a)

$$R_x \Gamma_y^{as} R_x = -\Gamma_y^{as}, \tag{C4b}$$

$$R_{\nu}\Gamma_{\nu}^{as}R_{\nu} = -\Gamma_{\nu}^{as}, \qquad (C4c)$$

$$R_{y}\Gamma_{y}^{as}R_{y} = \Gamma_{y}^{as}.$$
 (C4d)

From this follows

$$\Gamma_{x}^{\text{thick}} = \begin{pmatrix} 0 & \Gamma_{xxy} & 0 \\ \Gamma_{xxy} & 0 & \Gamma_{xyz} \\ 0 & -\Gamma_{xyz} & 0 \end{pmatrix},$$

$$\Gamma_{y}^{\text{thick}} = \begin{pmatrix} \Gamma_{yxx} & 0 & -\Gamma_{yzx} \\ 0 & \Gamma_{yyy} & 0 \\ \Gamma_{yzx} & 0 & \Gamma_{yzz} \end{pmatrix}.$$
(C5)

2. Thin slab

We now work in the basis of the thin slab, depicted in Fig. 2(c). We now consider the full heterostructure Hamiltonian (12).

$$H_{\chi m} = \chi v \mathbf{p} \cdot \mathbf{\sigma} + \begin{cases} -\chi m \, \mathbf{\sigma} \cdot \mathbf{\alpha}_2 & z < 0 \\ 0 & 0 < z < W, \\ \chi m \, \mathbf{\sigma} \cdot \mathbf{\beta}_2 & z > W \end{cases}$$
(C6)

with $m \to \infty$. The behavior under reflections and TR is as in the previous section but now with two TR-breaking magnetizations.

We consider two symmetry transformations. First we note that the combined reflection R_z , which swaps the top and bottom surfaces, and R_y , which interchanges $\sigma \cdot \alpha_2$ and $\sigma \cdot \beta_2$, leave the Hamiltonian invariant. Second, the combination of R_x and R_y inverts both $\sigma \cdot \alpha_2$ and $\sigma \cdot \beta_2$, which can be compensated by $m \rightarrow -m$. Altogether,

$$R_{\nu}R_{z}H_{\chi m}R_{z}R_{\nu} = H_{\chi m}, \qquad R_{x}R_{\nu}H_{\chi m}R_{\nu}R_{x} = H_{\chi - m}.$$
 (C7)

Both the symmetric and the antisymmetric parts of the response tensor thus satisfy

$$R_{\rm v}R_{\rm z}\Gamma_{\rm x}R_{\rm z}R_{\rm v}=\Gamma_{\rm x},$$
 (C8a)

The response tensor due to the bottom arc is

$$R_{\nu}R_{z}\Gamma_{\nu}R_{z}R_{\nu} = -\Gamma_{\nu},$$
 (C8b)

and, since the symmetric part is odd under $m \to -m$, it satisfies

$$R_x R_y \Gamma_x^s R_y R_x = \Gamma_x^s,$$
 (C9a)

$$R_x R_y \Gamma_y^s R_y R_x = \Gamma_y^s, \tag{C9b}$$

while the antisymmetric part satisfies

$$R_x R_y \Gamma_x^{as} R_x R_y = -\Gamma_x^{as}, \qquad (C10a)$$

$$R_x R_y \Gamma_y^{as} R_x R_y = -\Gamma_y^{as}. \tag{C10b}$$

From this follows.

$$\Gamma_x^{\text{thin}} = \begin{pmatrix} \Gamma_{xxx} & 0 & 0\\ 0 & \Gamma_{xyy} & \Gamma_{xyz}\\ 0 & -\Gamma_{xyz} & \Gamma_{xzz} \end{pmatrix},$$

$$\Gamma_y^{\text{thin}} = \begin{pmatrix} 0 & \Gamma_{yxy} & -\Gamma_{yzx}\\ \Gamma_{yxy} & 0 & 0\\ \Gamma_{yzx} & 0 & 0 \end{pmatrix}.$$
(C11)

Finally, we may also constrain the dependency of the components with respect to the angle $\Delta=(\beta-\alpha)/2\in[-\pi,\pi]$. In terms of Δ , the magnetization directions are given by $\alpha_2=(-\sin\Delta,\cos\Delta)$ and $\beta_2=(\sin\Delta,\cos\Delta)$. First, note that the transformation $\Delta\to-\Delta$ may be compensated by R_x . From this follows that components of the symmetric part of Γ are odd under $\Delta\to-\Delta$ while components of the anti-symmetric part are even. Next note, that $\Delta\to\Delta+\pi$ inverts both magnetizations and may be compensated by TR. From this follows that components of the symmetric part of Γ are odd under $\Delta\to\Delta+\pi$ while components of the antisymmetric part are even.

APPENDIX D: PHOTOGALVANIC CURRENT DUE TO ARC-BULK EXCITATIONS

As explained in the main text, the leading-order current contribution due to arc-bulk excitations is of the same order of magnitude as the subleading contributions from bulk-bulk excitations. Other types of finite-size corrections that we had to account for when considering bulk-bulk excitations can now be disregarded, as they would give corrections of higher order. In particular, we can replace the momentum sum over p_z by integrals in both the thick and thin slab regimes. Furthermore, we can assume $W \to \infty$ and $\delta \to \infty$ in both regimes and neglect the finite light momentum k. In the thick-slab limit only the bottom arc is relevant, in the thin-slab limit both arcs contribute.

$$\Gamma_{ij}^{ab,b} = \frac{8\eta\tau}{W} \int \frac{d^3p}{p} \Theta(p_z) \Theta(p_y) \left\{ \Theta(-\chi p_x) \delta(1 - p + \chi p_x) \left[\frac{\boldsymbol{p}_{\parallel}}{p} - \chi \boldsymbol{\alpha}_1 \right] M_i^{ab,b,+} \left(\boldsymbol{M}_j^{ab,b,+} \right)^* + \Theta(\chi p_x) \delta(1 - \chi p_x - p) \left[\chi \boldsymbol{\alpha}_1 + \frac{\boldsymbol{p}_{\parallel}}{p} \right] M_i^{ab,b,-} \left(\boldsymbol{M}_j^{ab,b,-} \right)^* \right\}$$
(D1)

where all momenta are dimensionless (in the Appendix we suppress the tilde, which denotes dimensionless units in the main text). The first line captures transitions between conduction band and arc sheet, while the second captures transitions between the arc

sheet and the valence band (the first Heaviside- Θ function enforces normalizability of the arc states, the second allows transitions between empty and occupied states only). We also defined the arc-bulk matrix elements [$\mathbf{p} = p(\sin\theta\cos\phi, \sin\theta\sin\phi, \cos\theta)$]

$$\mathbf{M}^{\mathrm{ab,b,+}} = \sqrt{Wp} \langle \mathrm{bulk}, +, \mathbf{p} | \mathbf{\sigma} | \mathrm{arc,b}, \mathbf{p}_{\parallel} \rangle = \sqrt{\frac{2 \sin \theta \sin \phi}{1 - \chi \sin \theta \cos \phi}} \frac{\cos \theta (-\mathbf{\alpha}_2 - i\hat{\mathbf{z}})}{\chi + \sin \theta \cos \phi}, \tag{D2a}$$

$$\mathbf{M}^{\mathrm{ab,b,-}} = \sqrt{Wp} \langle \mathrm{arc,b}, \mathbf{p}_{\parallel} | \mathbf{\sigma} | \mathrm{bulk}, -, \mathbf{p} \rangle = \sqrt{\frac{2 \sin \theta \sin \phi}{1 + \chi \sin \theta \cos \phi}} \frac{\cos \theta (\mathbf{\alpha}_2 - i\hat{\mathbf{z}})}{\chi - \sin \theta \cos \phi}. \tag{D2b}$$

Letting $p_x \to -p_x$ in the second term of Eq. (D1) the current may be written as

$$\Gamma_{ij}^{\text{ab,b}} = \frac{16\eta\tau}{\tilde{W}} \int \frac{d^3p}{p} \Theta(\cos\theta) \Theta(\sin\phi) \Theta(-\chi\cos\phi) \frac{\delta(1-p(1-\chi\sin\theta\cos\phi))\cos^2\theta\sin\theta\sin\phi}{(1-\chi\sin\theta\cos\phi)(1+\chi\sin\theta\cos\phi)^2} \times \left\{ \left(\frac{\sin\theta\cos\phi - \chi}{\sin\theta\sin\phi}\right) (\alpha_2 + i\hat{z})_i (\alpha_2 - i\hat{z})_j + \left(\frac{-\sin\theta\cos\phi + \chi}{\sin\theta\sin\phi}\right) (\alpha_2 - i\hat{z})_i (\alpha_2 + i\hat{z})_j \right\}. \tag{D3}$$

This may be evaluated straightforwardly. The resulting response tensor in the thick slab basis is

$$\Gamma_x^{\text{ab,thick}} = \Gamma_x^{\text{ab,b}} = \frac{\eta \tau}{W} \begin{pmatrix} 0 & 0 & 0 \\ 0 & 0 & i \frac{16\pi}{3} \chi \\ 0 & -i \frac{16\pi}{3} \chi & 0 \end{pmatrix}, \quad \Gamma_y^{\text{ab,thick}} = \Gamma_y^{\text{ab,b}} = \frac{\eta \tau}{W} \begin{pmatrix} 0 & 0 & 0 \\ 0 & 2\pi \ln 2 & 0 \\ 0 & 0 & 2\pi \ln 2 \end{pmatrix}. \tag{D4}$$

The current due to the top arc (present only in the thin slab regime) may be obtained analogously. The result for the top arc in the basis $\hat{x} = \beta_1$, $\hat{y} = \beta_2$ is

$$\Gamma_{x}^{\text{ab,t}} = \frac{\eta \tau}{W} \begin{pmatrix} 0 & 0 & 0 \\ 0 & 0 & i \frac{16\pi}{3} \chi \\ 0 & -i \frac{16\pi}{3} \chi & 0 \end{pmatrix}, \quad \Gamma_{y}^{\text{ab,t}} = -\frac{\eta \tau}{W} \begin{pmatrix} 0 & 0 & 0 \\ 0 & 2\pi \ln 2 & 0 \\ 0 & 0 & 2\pi \ln 2 \end{pmatrix}. \tag{D5}$$

In the thin-slab case both contributions combine into the total arc-bulk contribution. Introducing the rotation operator

$$R(\varphi) = \begin{pmatrix} \cos \varphi & -\sin \varphi & 0\\ \sin \varphi & \cos \varphi & 0\\ 0 & 0 & 1 \end{pmatrix},\tag{D6}$$

the total arc-bulk contribution, in the thin-slab basis [Fig. 2(c)], is given by

$$\Gamma_{abc}^{\text{ab,thin}} = R(\Delta)_{ai} R(\Delta)_{bj} R(\Delta)_{ck} \Gamma_{ijk}^{\text{ab,t}} + R(-\Delta)_{ai} R(-\Delta)_{bj} R(-\Delta)_{ck} \Gamma_{ijk}^{\text{ab,b}}, \tag{D7}$$

which evaluates to

$$\frac{\mathbf{\Gamma}^{\text{ab,thin}}}{4\pi \, \eta \tau / W} = \hat{\boldsymbol{x}} \begin{pmatrix} \ln 2 \, \sin^3 \Delta & 0 & 0 \\ 0 & \ln 2 \, \sin \Delta \, \cos^2 \Delta & i \frac{8}{3} \chi \, \cos^2 \Delta \\ 0 & -i \frac{8}{3} \chi \, \cos^2 \Delta & \ln 2 \, \sin \Delta \end{pmatrix} + \hat{\boldsymbol{y}} \, \sin \Delta \begin{pmatrix} 0 & \ln 2 \, \cos^2 \Delta & -i \frac{8}{3} \chi \, \sin \Delta \\ \ln 2 \, \cos^2 \Delta & 0 & 0 \\ i \frac{8}{3} \chi \, \sin \Delta & 0 & 0 \end{pmatrix}. \quad (D8)$$

APPENDIX E: PHOTOGALVANIC CURRENT DUE TO BULK-BULK EXCITATIONS

This Appendix section is structured as follows. First we perform some general manipulations. Next we discuss the thick- and thin-slab limits separately. In the thick-slab limit, we may let $W \to \infty$ and ignore the quantization condition Eq. (8). Corrections to the infinite system response arise from the spatial variation of the electromagnetic field corresponding to finite k, $1/\delta$. These are of the same order of magnitude as the current due to arc-bulk excitations. Conversely, in the thin-slab limit, the spatial dependence of the electromagnetic field may be ignored (k = 0, $1/\delta = 0$), but the quantization condition due to finite W leads to corrections of the same order as the arc-bulk current.

We start from Eq. (22) and specify to bulk states m = (p, +) and n = (q, -),

$$\Gamma_{ij}^{bb} = \frac{8\pi \eta \tau}{\tilde{W}^3} \int d^2 \tilde{p}_{\parallel} \sum_{\tilde{p}_z \tilde{q}_z} (\hat{\boldsymbol{v}}_{\boldsymbol{p}+} + \hat{\boldsymbol{v}}_{\boldsymbol{q}-}) \delta(1 - \tilde{p} - \tilde{q}) \left[\tilde{\boldsymbol{M}}^{bb} \otimes \left(\tilde{\boldsymbol{M}}^{bb} \right)^* \right]_{ij} \bigg|_{\boldsymbol{q}_{\parallel} = \boldsymbol{p}_{\parallel} - \boldsymbol{k}_{\parallel}}$$
(E1)

where we defined the dimensionless bulk-bulk matrix elements

$$\tilde{\boldsymbol{M}}^{\mathrm{bb}} = \tilde{W} \langle \mathrm{bulk}, +, \tilde{\boldsymbol{p}} | \boldsymbol{\sigma} e^{i\tilde{z}\tilde{k}_{z} - \tilde{z}/\tilde{\delta}} | \mathrm{bulk}, -, \tilde{\boldsymbol{q}} \rangle. \tag{E2}$$

Note that as opposed to the main text here we explicitly include the light momentum k. Since $k = \omega/c$, the light momentum is a factor v/c smaller than the typical momenta of excited states $\sim 1/\ell = \omega/v$. We will show below that it does not contribute at the

relevant order of magnitude, in agreement with the argumentation in the main text. We set $\mathbf{k} = (k_{\parallel} \cos \gamma, k_{\parallel} \sin \gamma, k_z)$ and keep terms to first order in \tilde{k}_z , $\tilde{k}_{\parallel} \sim v/c$.

We proceed by performing the integral over p_{\parallel} using the conservation of energy. The delta function gives the condition

$$g(p_{\parallel}) = 1 - \sqrt{p_{\parallel}^2 + p_z^2} - \sqrt{p_{\parallel}^2 + q_z^2 - 2p_{\parallel}k_{\parallel}\cos(\phi - \gamma) + k_{\parallel}^2} = 0.$$

This has a real solution if, to leading order in k_{\parallel} ,

$$p_z + q_z < 1 \text{ or } P < 1/2,$$
 (E3)

where we defined new variables

$$P = \frac{1}{2}(p_z + q_z), \ Q = \frac{1}{2}(p_z - q_z)$$
 (E4)

with P > 0, P > Q > -P. The solution to $g(p_{\parallel}) = 0$ is given by

$$p_{\parallel} = \frac{1}{2}\sqrt{(1 - 4P^2)(1 - 4Q^2)} + \frac{k_{\parallel}}{2}\cos(\phi - \gamma)(1 + 4PQ). \tag{E5}$$

Performing the integration over p_{\parallel} also gives rise to the Jacobian factor

$$\frac{1}{|g'(p_{\parallel})|} = \left[\frac{p_{\parallel} + p_z (dp_z/dp_{\parallel})}{p} + \frac{p_{\parallel} + q_z (dq_z/dp_{\parallel}) - k_{\parallel} \cos(\phi - \gamma)}{q} \right]^{-1}.$$
 (E6)

The derivatives dp_z/dp_{\parallel} may be obtained from the boundary condition Eq. (A4). They contribute at order 1/W. Altogether, the bulk-bulk response tensor is now

$$\Gamma_{ijk}^{bb} = \frac{8\pi \eta \tau}{W^3} \int d\phi \sum_{p_z q_z} \frac{p_{\parallel}}{|g'(p_{\parallel})|} (\hat{\mathbf{v}}_{p+} + \hat{\mathbf{v}}_{q-})_i M_j^{bb} (M_k^{bb})^* \Theta[1 - p_z - q_z] \bigg|_{p_{\parallel} = p_{\parallel}(p_z, q_z, \phi), \ \mathbf{q}_{\parallel} = \mathbf{p}_{\parallel} - \mathbf{k}_{\parallel}}.$$
(E7)

Next, consider the matrix elements, M_i^{bb} . We can split them into a normalization factor that is common to all M_i and a factor that depends on i,

$$M_i^{\text{bb}} = W \langle \text{bulk}, +, \boldsymbol{p} | \sigma_i e^{ik_z z - z/\delta} | \text{bulk}, -, \boldsymbol{q} \rangle = \frac{1}{\sqrt{N_{\boldsymbol{p}} + N_{\boldsymbol{q}}}} \mathcal{M}_i, \tag{E8}$$

where the $N_{p\pm}$ are defined in Eq. (A10). Using

$$\langle \alpha_{+} | \boldsymbol{\sigma} | \alpha_{+} \rangle = -\langle \alpha_{-} | \boldsymbol{\sigma} | \alpha_{-} \rangle = \boldsymbol{\alpha}_{1}, \ \langle \alpha_{+} | \boldsymbol{\sigma} | \alpha_{-} \rangle = \langle \alpha_{-} | \boldsymbol{\sigma} | \alpha_{+} \rangle^{*} = i\boldsymbol{\alpha}_{2} + \hat{\boldsymbol{z}}, \tag{E9}$$

the \mathcal{M}_i read

$$\mathcal{M} = \{ p_z q_z I_1 + [p_2 q_2 + (p - \chi p_1)(q + \chi q_1)] I_2 - (p_z q_2 I_3 + p_2 q_z I_4) \} \alpha_1$$

$$+ \{ [\chi \cdot (pq_2 - p_2 q) - (p_1 q_2 + p_2 q_1)] I_2 + (p_z q_1 I_3 + p_1 q_z I_4) + \chi (p_z q I_3 - p q_z I_4) \} \alpha_2$$

$$+ i \{ [\chi (pq_2 + p_2 q) - (p_1 q_2 - p_2 q_1)] I_2 - (p_z q_1 I_3 - p_1 q_z I_4) - \chi (p_z q I_3 + p q_z I_4) \} \hat{\mathbf{z}},$$
(E10)

where we defined $x_i = \alpha_i \cdot x$ as well as the integrals

$$I_{1} = \int_{0}^{W} dz \, e^{(ik_{z} - 1/\delta)z} \cos p_{z} z \cos q_{z} z, \quad I_{2} = \int_{0}^{W} dz \, e^{(ik_{z} - 1/\delta)z} \sin p_{z} z \sin q_{z} z, \tag{E11a}$$

$$I_{3} = \int_{0}^{W} dz \, e^{(ik_{z} - 1/\delta)z} \cos p_{z} z \sin q_{z} z, \quad I_{4} = \int_{0}^{W} dz \, e^{(ik_{z} - 1/\delta)z} \sin p_{z} z \cos q_{z} z. \tag{E11b}$$

These lead to conservation of "momentum" perpendicular to the boundary if W or δ become large. It will prove convenient to also define the combinations

$$I_{+} = p_{z}I_{3} \pm q_{z}I_{4} = P(I_{3} \pm I_{4}) + Q(I_{3} \mp I_{4}),$$
 (E12)

To leading order in k_{\parallel} , this gives

$$p_z q I_3 \pm p q_z I_4 = \frac{1}{2} [I_{\pm} - (4PQ + 2\mathbf{k}_{\parallel} \cdot \mathbf{p}_{\parallel}) I_{\mp}].$$
 (E13)

1. Thick slab $W \gg \delta$

In this limit, dominant corrections are of order $1/\delta$. They stem from the light penetration depth $\delta = 1$ and the finite light momentum k with $k \sim 1/\delta$. Ignoring the quantization of p_z , q_z , which give corrections of order $1/W \ll 1/\delta$ we replace

$$\sum_{p,q_z} \to \int_0^\infty dp_z \int_0^\infty dq_z \to \frac{2W^2}{\pi^2} \int_0^\infty dP \int_{-P}^P dQ. \tag{E14}$$

We expand the bulk-bulk current in orders of $1/\delta$ and k_i .

a. Leading order bulk-bulk contributions ($\Gamma^{bb,thick}$)

For the leading-order contributions we set $k_{\parallel} = 0$ (i.e., $p_{\parallel} = q_{\parallel}$) and analyze integrals of the type

$$\int_0^{1/2} dP \int_{-P}^P dQ \, I_i I_j^* f(P, Q), \tag{E15}$$

which enter the current formula with a smooth kernel $f(P,Q) \sim \partial_{P,Q} f(P,Q) \sim 1$ (f does not depend on the small parameter). Considering i = j = 1, we find

$$|I_1|^2 \simeq \frac{4(\delta^{-2} + k_z^2)(P^2 + Q^2)^2}{(\delta^{-2} + (k_z - 2P)^2)(\delta^{-2} + (k_z + 2P)^2)(\delta^{-2} + (k_z - 2Q)^2)(\delta^{-2} + (k_z + 2Q)^2)}.$$
 (E16)

The leading contribution after integration is the term proportional to P^4 . Next, we use that

$$\int_{-\infty}^{\infty} dQ \frac{4(k_z^2 + \delta^{-2})}{(\delta^{-2} + (k_z - 2Q)^2)(\delta^{-2} + (k_z + 2Q)^2)} = \pi \delta,$$
(E17)

so that to leading order in k_z and $1/\delta$ we can simplify

$$\frac{4(k_z^2 + \delta^{-2})}{\left(\delta^{-2} + (k_z - 2Q)^2\right)(\delta^{-2} + (k_z + 2Q)^2)} \to (\pi\delta)\delta(Q).$$
 (E18)

 $|I_2|^2$ and $I_1I_2^*$ are similar to $|I_1|^2$ with $(P^2+Q^2)^2$ replaced by $(P^2-Q^2)^2$ or (P^4-Q^4) , respectively. They clearly give the same leading order behavior. For $P\gg v/c$ we have to leading order

$$|I_1|^2 \simeq |I_2|^2 \simeq I_1 I_2^* \simeq \frac{\pi \delta}{16} \delta(Q).$$
 (E19)

Since f(P, Q) is smooth, corrections from small $P \sim v/c$ are of higher order in v/c.

Consider next $|I_{\pm}|^2$ and the corresponding cross-term. It is

$$|I_{+}|^{2} \simeq \frac{4(\delta^{-2} + k_{z}^{2})^{2}(P^{2} + Q^{2})^{2}}{(\delta^{-2} + (k_{z} - 2P)^{2})(\delta^{-2} + (k_{z} + 2P)^{2})(\delta^{-2} + (k_{z} - 2Q)^{2})(\delta^{-2} + (k_{z} + 2Q)^{2})} \simeq \frac{\pi(\delta^{-2} + k_{z}^{2})\delta}{16}\delta(Q). \tag{E20}$$

Due to the extra factor of $\delta^{-2} + k_z^2$ this may safely be ignored. However,

$$|I_{-}|^{2} \simeq \frac{64P^{2}Q^{2}(P^{2} - Q^{2})^{2}}{(\delta^{-2} + (k_{z} - 2P)^{2})(\delta^{-2} + (k_{z} + 2P)^{2})(\delta^{-2} + (k_{z} - 2Q)^{2})(\delta^{-2} + (k_{z} + 2Q)^{2})}$$
(E21)

does not come with a small factor in the numerator at all. Naively one might expect a contribution of order δ^3 . The factor of Q^2 reduces this to a contribution of order δ . The leading order contribution stems from the lowest power in Q, i.e., the term proportional to P^6Q^2 . Then, integrating by parts

$$\int_{-P}^{P} dQ \frac{64Q^{2} f(P,Q)}{(\delta^{-2} + (k_{z} - 2Q)^{2})(\delta^{-2} + (k_{z} + 2Q)^{2})} = -\frac{4\delta}{k_{z}} \int_{-P}^{P} dQ \, Q f(P,Q) \partial_{Q} \left[\frac{\pi}{2} - \arctan\left(\frac{\delta^{-2} - k_{z}^{2} + 4Q^{2}}{2k_{z}/\delta} \right) \right]$$

$$= 4\pi \delta \left\{ P[f(P,-P) - f(P,P)] \delta(P) + \int_{-P}^{P} dQ \, [f(P,Q) + Q \partial_{Q} f(P,Q)] \delta(Q) \right\}$$

$$= 4\pi \delta f(P,0) \tag{E22}$$

Here, we used

$$\frac{1}{k_z} \int_{-\infty}^{\infty} dQ \left[\frac{\pi}{2} - \arctan\left(\frac{\delta^{-2} - k_z^2 + 4Q^2}{2k_z/\delta}\right) \right] = \pi,$$

so that the integrand is again a delta function for k_z , $1/\delta \to 0$. Hence, for $P \gg v/c$

$$|I_{-}|^{2} \simeq \frac{\pi \delta}{4} P^{2} \delta(Q).$$
 (E23)

For the cross term we find by a similar argument

$$I_{+}I_{-}^{*} \simeq -\frac{\pi (k_{z} + i/\delta)^{2}}{16} \delta P \partial_{Q} \delta(Q), \tag{E24}$$

which is again negligible.

Finally, consider cross terms of the type $I_1I_+^*$, $I_2I_+^*$, $I_1I_-^*$, $I_2I_-^*$. The former two read to leading order

$$I_{i}I_{+}^{*} \simeq \frac{4(k_{z}^{2} + \delta^{-2})(\delta^{-1} + ik_{z})P^{4}}{(\delta^{-2} + (k_{z} - 2P)^{2})(\delta^{-2} + (k_{z} + 2P)^{2})(\delta^{-2} + (k_{z} - 2Q)^{2})(\delta^{-2} + (k_{z} + 2Q)^{2})} \simeq \frac{\pi(\delta^{-1} + ik_{z})}{16}\delta \delta(Q). \tag{E25}$$

The latter two read

$$I_{i}I_{-}^{*} \simeq \frac{-16(1/\delta - ik_{z})P^{5}Q}{(\delta^{-2} + (k_{z} - 2P)^{2})(\delta^{-2} + (k_{z} + 2P)^{2})(\delta^{-2} + (k_{z} - 2Q)^{2})(\delta^{-2} + (k_{z} + 2Q)^{2})} \simeq \frac{\pi(k_{z}\delta - i)}{16}P\partial_{Q}\delta(Q). \tag{E26}$$

With this we can now easily calculate the bulk-bulk current in the thick-slab limit at leading order. We drop all combinations $I_iI_j^*$ with $i, j \in \{1, 2, +, -\}$, which do not give a order- δ contribution. The remaining combinations all give a delta function $\delta(Q)$, corresponding to conservation of perpendicular momentum, $p_z = q_z$, and hence p = q = 1/2 and $p_{\parallel} = \sqrt{1 - 4P^2}/2 = \sqrt{1 - p_z^2}/2$. Identifying the combinations $I_iI_j^*$ giving rise to order- δ terms motivates the following definition:

$$\mathcal{M} \simeq \Sigma_0 \mathcal{I}_0 + \Sigma_1 \mathcal{I}_1,$$
 (E27)

where $\mathcal{I}_0 \simeq 2p^2I_1 \simeq 2p^2I_2$ and $\mathcal{I}_1 = p^2I_-/P$. Here Σ_0 is (up to normalization) the matrix element at fixed momentum,

$$\Sigma_0 \equiv (1 - \sin^2 \theta \cos^2 \phi) \alpha_1 - \sin^2 \theta \cos \phi \sin \phi \alpha_2 + i \chi \sin \theta \sin \phi \hat{z} \propto \langle +, p | \sigma | -, p \rangle, \tag{E28}$$

in terms of the spherical coordinates $p_z = p \cos \theta$, $p_{\parallel} = p \sin \theta$, while

$$\Sigma_1 \equiv \chi \cos \theta \, \alpha_2 - i \cos \theta \sin \theta \cos \phi \, \hat{z}.$$

This term in the matrix element only arises if one allows for $p_z \neq q_z$. It arises because $I_{3,4}$ may become large if $p_z - q_z \sim 1/\delta$ even though they vanish for $p_z = q_z$ (or $p_z - q_z \sim 1/W$ if the integral is cut off by the thickness of the slab, see below). The normalization factor evaluates to

$$\frac{1}{N_{p+}N_{p-}} = \frac{1}{p^4(1-\sin^2\theta\cos^2\phi)}.$$
 (E29)

Altogether, after transforming $P = (\cos \theta)/2$, we have

$$\Gamma_{0,ij}^{bb,thick} = \frac{\eta \tau \delta}{W} \int d\Omega \frac{\Theta(\cos\theta) \left(\frac{\cos\phi}{\sin\phi}\right) \sin\theta}{1 - \sin^2\theta \cos^2\phi} \left\{ \Sigma_{0,i} \Sigma_{0,j}^* + \Sigma_{1,i} \Sigma_{1,j}^* \right\}.$$
 (E30)

The angular integrals may be evaluated straightforwardly. This gives Eq. (40). Note that the result is symmetric under rotations in the x, y plane and thus independent of the direction of the boundary conditions.

b. Subleading order bulk-bulk contributions ($\delta\Gamma^{bb,thick}$)

We now consider the leading corrections δJ^{bb} to J^{bb} . From the above calculations, one can expect a correction of order

$$\frac{\delta\Gamma^{\rm bb}}{\Gamma^{\rm bb}} \sim \frac{v}{c} \ll 1.$$
 (E31)

stemming from two different sources: First, from an in-plane momentum shift due to the finite light momentum k_{\parallel} , and second, from the corrections to the integrals $I_iI_j^*$ of order $(1/\delta)^0$, k_z^0 . Consider first corrections due to finite light momentum. Since these are already of the same magnitude as the corrections due to finite-size as well as the arc-bulk current, one may ignore the slab geometry here. It is straightforward to verify that for a bulk Weyl cone these corrections vanish. We thus expect that the relevant corrections due to a finite k vanish also in the slab. We first consider finite k_{\parallel} . The products $I_iI_j^*$ do not involve k_{\parallel} and are thus approximated as in the leading-order calculation above. In \mathcal{M} we can thus again separate out $\mathcal{I}_0 \simeq 2p^2I_1 \simeq 2p^2I_2$ and $\mathcal{I}_1 = p^2I_-/P$ and expand the prefactors up to leading order in k_{\parallel} ,

$$\mathcal{M} \simeq \Sigma_0' \mathcal{I}_0 + \Sigma_1' \mathcal{I}_1$$
, where $\Sigma_i' = \Sigma_i + k_{\parallel} \delta \Sigma_i + \mathcal{O}(k_{\parallel}^2)$, (E32)

where, introducing the shorthand notation $c_x = \cos x$, $s_x = \sin x$,

$$\delta \mathbf{\Sigma}_{0} = \frac{1}{2} \left[\left(\chi s_{\theta}^{2} c_{\phi}^{2} + 2s_{\theta} c_{\phi} s_{\phi}^{2} - \chi \right) c_{\gamma} + c_{\phi} s_{\phi} \left(\chi s_{\theta}^{2} - 2s_{\theta} c_{\phi} \right) s_{\gamma} \right] \boldsymbol{\alpha}_{1}$$

$$+ \frac{1}{2} \left[c_{\phi} s_{\phi} \left(\chi s_{\theta}^{2} - 2s_{\theta} c_{\phi} \right) c_{\gamma} + \left(\chi s_{\theta}^{2} s_{\phi}^{2} - 2s_{\theta} c_{\phi} s_{\phi}^{2} - \chi \right) s_{\gamma} + s_{\theta} s_{\phi + \gamma} \right] \boldsymbol{\alpha}_{2} - \frac{i}{2} s_{\gamma - \phi} [s_{\theta} - \chi c_{\phi}] \hat{\boldsymbol{z}},$$
 (E33a)

TABLE III. Estimated inaccuracy of numerical results for the subleading bulk-bulk response tensor $\delta\Gamma^{bb}$. The error corresponds to the statistical relative standard error of a fit with first-order polynomial in $1/\delta$ and $\delta \in \{10^{2.8}, 10^{3.0}, ..., 10^{3.4}\}$ (for larger values of δ the integration is no longer stable due to the sharply peaked nature of the integrals I_i). Use of higher-order polynomials or inclusion of smaller δ points gives comparable results and deviations.

	$\delta\Gamma_{xxy}^{ m bb}$	$\delta\Gamma_{xyz}^{ m bb}$	$\delta\Gamma^{ m bb}_{yxx}$	$\delta\Gamma^{ m bb}_{yyy}$	$\delta\Gamma^{ m bb}_{yzz}$	$\delta\Gamma^{ m bb}_{yzx}$
Error	5×10^{-4}	3×10^{-3}	5×10^{-5}	5×10^{-3}	1×10^{-3}	1×10^{-5}

$$\delta \mathbf{\Sigma}_1 = \frac{1}{2} \left\{ s_{\gamma} \boldsymbol{\alpha}_1 - c_{\gamma} \boldsymbol{\alpha}_2 + i \left[-\left(s_{\phi}^2 + \chi s_{\theta} c_{\phi} \right) c_{\gamma} + \left(s_{\phi} c_{\phi} - \chi s_{\theta} s_{\phi} \right) s_{\gamma} \right] \hat{\boldsymbol{z}} \right\}. \tag{E33b}$$

Other terms entering the current formula expand as

$$\frac{p_{\parallel}}{|g'(p_{\parallel})|}(\hat{\boldsymbol{v}}_{p+} + \hat{\boldsymbol{v}}_{q-}) = \frac{s_{\theta}}{2} \binom{c_{\phi}}{s_{\phi}} + \frac{k_{\parallel}}{2} \binom{c_{\gamma-2\phi}}{-s_{\gamma-2\phi}} + \mathcal{O}(k_{\parallel}^2), \tag{E34a}$$

$$N_{p+}N_{p-} = \frac{1}{16} \left(1 - s_{\theta}^2 c_{\phi}^2 \right) + \frac{k_{\parallel}}{8} \left[(s_{\theta} c_{\phi} - \chi) c_{\gamma} + (\chi s_{\theta} - c_{\phi}) s_{\theta} c_{\phi} c_{\gamma - \phi} \right] + \mathcal{O}(k_{\parallel}^2). \tag{E34b}$$

We now specify to the basis of the thick slab, $\hat{x} = \alpha_1$, $\hat{y} = \alpha_2$. For $\gamma = 0$ (i.e., $k_{\parallel} = k_{\parallel}\hat{x}$) this combines to the total correction of the response tensor

$$\delta\Gamma_{x}^{\mathrm{bb},k_{\parallel}} \propto \int_{0}^{\frac{\pi}{2}} d\theta \int_{0}^{2\pi} d\phi \begin{pmatrix} c_{\theta}^{2} - 4s_{\theta}^{2}s_{\phi}^{4} + (5s_{\theta}^{2} - 2)s_{\phi}^{2} & 2s_{\theta}^{2}c_{\phi}s_{\phi}(2s_{\phi}^{2} - 1) & is_{\theta}s_{\phi}(3s_{\phi}^{2} - 2) \\ 2s_{\theta}^{2}c_{\phi}s_{\phi}(2s_{\phi}^{2} - 1) & 1 + 4s_{\theta}^{2}s_{\phi}^{4} + (3c_{\theta}^{2} - 5)s_{\phi}^{2} & ic_{\phi}s_{\theta}(1 - 3s_{\phi}^{2}) \\ -is_{\phi}s_{\theta}(3s_{\phi}^{2} - 2) & -ic_{\phi}s_{\theta}(1 - 3s_{\phi}^{2}) & -s_{\theta}^{2}(2s_{\phi}^{2} - 1) \end{pmatrix}, \tag{E35a}$$

$$\delta\Gamma_{y}^{\mathrm{bb},k_{\parallel}} \propto \int_{0}^{\frac{\pi}{2}} d\theta \int_{0}^{2\pi} d\phi \begin{pmatrix} c_{\phi}s_{\phi}(2c_{\theta}^{2} + 4s_{\theta}^{2}s_{\phi}^{2}) & s_{\theta}^{2}s_{\phi}^{2}(4s_{\phi}^{2} - 3) & -3ic_{\phi}s_{\theta}s_{\phi}^{2} \\ s_{\theta}^{2}s_{\phi}^{2}(4s_{\phi}^{2} - 3) & c_{\phi}s_{\phi}(2 - 4s_{\theta}^{2}s_{\phi}^{2}) & is_{\theta}s_{\phi}(2 - 3s_{\phi}^{2}) \\ 3ic_{\phi}s_{\theta}s_{\phi}^{2} & is_{\theta}s_{\phi}(3s_{\phi}^{2} - 2) & 2s_{\theta}^{2}c_{\phi}s_{\phi} \end{pmatrix}. \tag{E35b}$$

$$\delta\Gamma_{y}^{\text{bb},k_{\parallel}} \propto \int_{0}^{\frac{\pi}{2}} d\theta \int_{0}^{2\pi} d\phi \begin{pmatrix} c_{\phi}s_{\phi}(2c_{\theta}^{2} + 4s_{\theta}^{2}s_{\phi}^{2}) & s_{\theta}^{2}s_{\phi}^{2}(4s_{\phi}^{2} - 3) & -3ic_{\phi}s_{\theta}s_{\phi}^{2} \\ s_{\theta}^{2}s_{\phi}^{2}(4s_{\phi}^{2} - 3) & c_{\phi}s_{\phi}(2 - 4s_{\theta}^{2}s_{\phi}^{2}) & is_{\theta}s_{\phi}(2 - 3s_{\phi}^{2}) \\ 3ic_{\phi}s_{\theta}s_{\phi}^{2} & is_{\theta}s_{\phi}(3s_{\phi}^{2} - 2) & 2s_{\theta}^{2}c_{\phi}s_{\phi} \end{pmatrix}.$$
 (E35b)

It is straightforward to confirm that these expressions vanish upon integration over ϕ . Similar expressions for $\gamma = \pi/2$ (i.e., $\mathbf{k}_{\parallel} = k_{\parallel} \hat{\mathbf{y}}$) also vanish.

The remaining corrections are corrections to the products I_iI_i , which have been discussed above, of order $(k_z \pm i/\delta)^0$. We verified numerically, that the correction due to a finite k_z vanishes as expected. Fitting the numerically evaluated response tensor (for $\delta \in \{10^2, 2 \times 10^2, ..., 10^3\}$) to an expansion up to second order in $1/\delta$ we find (rounding to the second decimal)

$$\delta\Gamma_{\chi}^{\text{bb,thick}} = \frac{\eta \tau}{\tilde{W}} \begin{pmatrix} 0 & 4.19 & 0\\ 4.19 & 0 & -16.75i\chi\\ 0 & 16.75i\chi & 0 \end{pmatrix}, \tag{E36a}$$

$$\delta\Gamma_{y}^{\text{bb,thick}} = \frac{\eta \tau}{\tilde{W}} \begin{pmatrix} -4.19 & 0 & 9.87i \chi \\ 0 & -4.20 & 0 \\ -9.87i \chi & 0 & -8.40 \end{pmatrix}.$$
 (E36b)

To estimate the accuracy of these results we compare the numerical values given here to those obtained by fitting expansions to higher order in $1/\delta$ as well as by adding/removing data points corresponding to the smallest values of δ . These changes in the fitting procedure lead to changes in the numerical coefficients of $\leq 0.5\%$. The error analysis is summarized in Table III.

2. Thin slab $\delta \gg W \gg \ell$

In this limit, the leading finite-size corrections are $\sim 1/W$, as discussed in the main text. Corrections due to the spatial variation of the external field, which we found to give corrections of order $\sim 1/\delta$, are thus negligible and we can set $k = 0, \delta \to \infty$. We now work in the basis of the thin slab.

a. Leading order $(\Gamma^{bb,thin})$

To calculate the leading-order response we disregard the quantization of p_z , q_z . Considering leading-order terms of the integral products I_iI_i , the dominant contributions read

$$I_1^2 \simeq I_2^2 \simeq I_1 I_2 \simeq \frac{\pi \tilde{W}}{8} \delta(Q), \ I_-^2 \simeq \frac{\pi \tilde{W} P^2}{2} \delta(Q),$$
 (E37)

all other combinations contribute only at higher order. Since the difference to the leading contribution of the thick-slab case is in the constant prefactor, the leading-order bulk-bulk contribution in the thin-slab limit is given by the thick-slab result replacing $\delta/2 \to W$. The final response tensor reads

$$\Gamma_{ijk}^{bb} = i\chi \frac{4\pi \eta \tau}{3} \varepsilon_{ijk} (1 - \delta_{i,z}). \tag{E38}$$

b. Subleading order $(\delta \Gamma^{bb,thin})$

The leading corrections to the bulk-bulk contribution in the thin-slab limit are of order 1/W. They can stem from the quantization of p_z , q_z , the associated corrections to the velocity in Eq. (A11), and the corrections $\delta N_{p\pm}$ to the wave function normalization. The current is given by Eq. (E7) with p_z , q_z solutions of

$$\sin \Delta = \frac{\tan(p_z W)}{p_z} [p_{\parallel} \cos \phi - \chi p \cos \Delta], \tag{E39a}$$

$$\sin \Delta = \frac{\tan(q_z W)}{q_z} [p_{\parallel} \cos \phi + \chi q \cos \Delta], \tag{E39b}$$

where we defined the characteristic angle

$$\Delta = \frac{\beta - \alpha}{2} \in [-\pi, \pi]. \tag{E40}$$

These expressions as well as the tensors below are in the basis of the thin slab. Note that energy conservation makes p_{\parallel} and thus also p and q depend on (p_z, q_z) . To evaluate the expression for the current for a given value of Δ we resort to numerics. We then attempt to extract the functional dependence of the nonzero tensor components by fitting appropriate polynomials in $\sin \Delta$ and

We briefly outline the numerical strategy employed to extract the response tensor. For ϕ integration at fixed W we employ standard numerical techniques relying on evaluation of the integrand for a discrete set of ϕ points. For each ϕ point we numerically determine all solutions to Eqs. (E39) in the region $p_z + q_z < 1$. To determine $\delta \Gamma^{bb}$ we evaluate Eq. (E7) at $W \in \{100, 150, 200, 250\}$ and subtract the leading-order term, Eq. (E38). We then fit to an expansion up to second order in 1/W and extract the coefficient of the 1/W term. In this way we determine all symmetry-allowed elements of $\delta\Gamma^{bb}$ for 30 values of $\Delta \in [0, \pi/2]$ (the intervals $[-\pi, 0]$ and $[\pi/2, \pi]$ may be obtained from symmetry considerations, see Sec. C). Finally, we fit the components of the symmetric part of the response tensor to each element to an appropriate expansion in Fourier modes,

$$\sum_{n \text{ odd}}^{n_{\text{max}}} a_n^{\text{s}} \sin(n\Delta),$$

where we exploit that they are odd under $\Delta \to -\Delta$ and $\Delta \to \Delta + \pi$. Similarly, we fit the components of the antisymmetric

$$a_0^{\mathrm{as}} + \sum_{n \text{ even}}^{n_{\mathrm{max}}} a_n^{\mathrm{as}} \cos(n\Delta),$$

where we use that they are even under the above transformations. We found that $n_{\text{max}} = 3$ gives sufficiently good results with higher-order coefficients satisfying $a_{n>3}/(\max a_{n\leqslant 3}) \lesssim 10^{-3}$. Rounding to 10^{-2} , the subleading order response tensor due to bulk-bulk excitations in the thin-slab limit is

$$\delta\Gamma_{x}^{bb,thin} = \frac{\eta \tau}{W} \begin{pmatrix} -14.14 \sin \Delta + 4.71 \sin 3\Delta & 0 & 0 \\ 0 & -21.47 \sin \Delta - 4.71 \sin 3\Delta & -i\chi(26.71 + 6.88 \cos 2\Delta) \\ 0 & i\chi(26.71 + 6.88 \cos 2\Delta) & -23.04 \sin \Delta \end{pmatrix}, \quad (E41a)$$

$$\delta\Gamma_{y}^{bb,thin} = \frac{\eta \tau}{W} \begin{pmatrix} 0 & 3.67 \sin \Delta - 4.71 \sin 3\Delta & i\chi(26.50 - 6.89 \cos 2\Delta) \\ -i\chi(26.50 - 6.89 \cos 2\Delta) & 0 \end{pmatrix}. \quad (E41b)$$

$$\delta\Gamma_{y}^{\text{bb,thin}} = \frac{\eta \tau}{W} \begin{pmatrix} 0 & 3.67 \sin \Delta - 4.71 \sin 3\Delta & i\chi(26.50 - 6.89 \cos 2\Delta) \\ 3.67 \sin \Delta - 4.71 \sin 3\Delta & 0 & 0 \\ -i\chi(26.50 - 6.89 \cos 2\Delta) & 0 & 0 \end{pmatrix}. \tag{E41b}$$

These results are accurate to the first decimal: the error estimates of the numerical integration scheme are on the order of 10^{-1} to 10^{-2} . Similarly, altering the fitting procedure (e.g., by fitting to a first order expansion in 1/W or by removing data points in W) leads to changes in the numerical coefficients on the order of roughly 10^{-2} with the largest changes, at about 1%, observed for the Δ -independent terms in the circular components. Note that averaging over $\Delta \in [-\pi, \pi]$ restores rotational symmetry around the z axis, which implies that the Δ -independent terms of Γ_{xyz} and Γ_{yzx} should actually be equal. Here, they differ by roughly 0.5%, consistent with our error estimate.

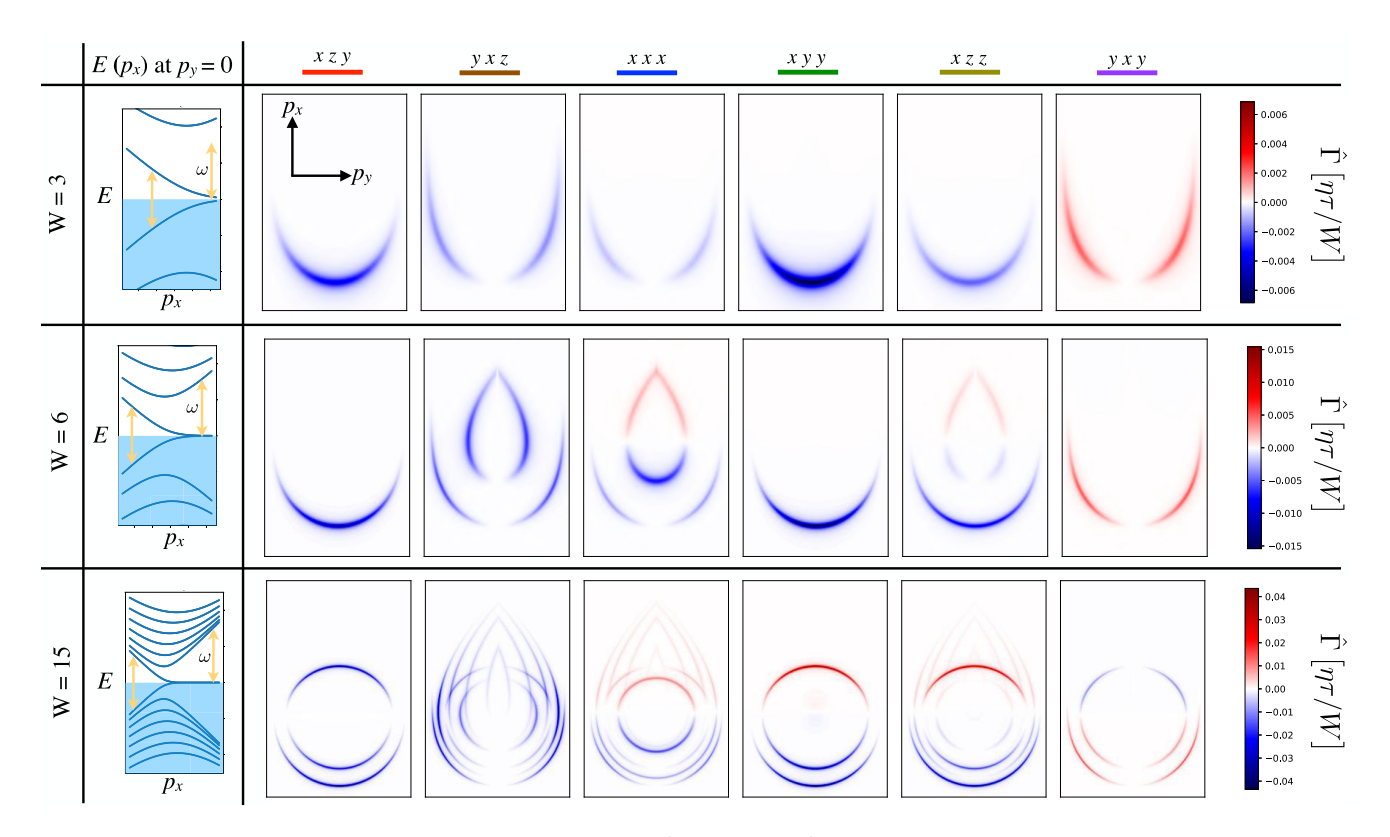


FIG. 8. Parallel-momentum (p_x, p_y) resolved response tensor $\hat{\Gamma}(\Gamma = \sum_{p_x, p_y} \hat{\Gamma})$ at three widths W = 3, 6, 15 for v = 1 and $\ell = 5$ sites. Left column indicates the dispersion at $p_y = 0$.

APPENDIX F: LATTICE SIMULATION OF A THIN SLAB

In this section we perform numerical calculations of the PGE response tensor for a lattice model of the Weyl slab in the thin-slab limit. It will extend the above semianalytical calculations, considered under the simplifying assumption $W\gg 1$ (the tilde is here still suppressed so that W is in units of ℓ), to the case of arbitrary W. In the *ultrathin* limit $W\sim 1$ the confinement-induced and bulk contributions are of the same order.

We consider the ultrathin limit using the lattice Hamiltonian,

$$H_{ij} = \frac{v}{2} [\sigma_x p_x + \sigma_y p_y + i\sigma_z \delta_{i,j+1} + \sigma_x (1 - \delta_{i,j+1})] + \text{H.c.},$$
(F1)

where i, j denote the site index at fixed in-plane momenta p_x , p_y . This lattice version of the original infinite-system Weyl Hamiltonian (lattice constant set to one) has been constructed replacing

$$\sigma_z p_z \mapsto \sigma_z \sin p_z + \sigma_x (\cos p_z - 1),$$
 (F2)

such that the Hamiltonians coincide at small p_z (the second term removes a spurious Weyl cone at $p_z = \pm \pi$). Transfor-

mation into the site basis replaces

$$\sin p_z \mapsto i\frac{1}{2}(\delta_{i,j+1} - \delta_{i,j-1}), \quad \cos p_z \mapsto \frac{1}{2}(\delta_{i,j+1} + \delta_{i,j-1}),$$
(F3)

which leads to (F1). The Hamiltonian (F1) can be considered for a finite site number. The choice of the Pauli matrix σ_x for the second term in (F2) sets the direction of the Fermi arc such that $\alpha_2 = \hat{x} = -\beta_2$, corresponding to $\Delta = \pi/2$ of the thin-slab case considered above [62].

Numerical results for the PGE response tensor in Eq. (22) are obtained via discretizing parallel momenta, numerically diagonalizing the Hamiltonian (F1), and summing over all pairs of states (one below and one above the Fermi level). The numerical discretization spacing and numerical broadening of the delta function expressing energy conservation have been decreased until convergence of the results. Figure 6 shows the results for the response tensor as a function of the width. Figure 8 shows the contributions resolved in the in-plane momentum. One can clearly see the cusp-like lines of the arc-bulk excitations and the circular lines of bulk-bulk excitations, c.f. Fig. 3. The signs of the contributions and the presence/absence of arc-bulk contributions is as discussed in the main text.

X. Wan, A. M. Turner, A. Vishwanath, and S. Y. Savrasov, Topological semimetal and Fermi-arc surface states in the electronic structure of pyrochlore iridates, Phys. Rev. B 83, 205101 (2011).

^[2] B. Q. Lv, H. M. Weng, B. B. Fu, X. P. Wang, H. Miao, J. Ma, P. Richard, X. C. Huang, L. X. Zhao, G. F. Chen, Z. Fang, X. Dai, T. Qian, and H. Ding, Experimental Discovery of Weyl Semimetal TaAs, Phys. Rev. X 5, 031013 (2015).

- [3] L. X. Yang, Z. K. Liu, Y. Sun, H. Peng, H. F. Yang, T. Zhang, B. Zhou, Y. Zhang, Y. F. Guo, M. Rahn *et al.*, Weyl semimetal phase in the non-centrosymmetric compound TaAs, Nat. Phys. 11, 728 (2015).
- [4] S.-Y. Xu, N. Alidoust, I. Belopolski, Z. Yuan, G. Bian, T.-R. Chang, H. Zheng, V. N. Strocov, D. S. Sanchez, G. Chang *et al.*, Discovery of a Weyl fermion state with Fermi arcs in niobium arsenide, Nat. Phys. 11, 748 (2015).
- [5] S.-Y. Xu, C. Liu, S. K. Kushwaha, R. Sankar, J. W. Krizan, I. Belopolski, M. Neupane, G. Bian, N. Alidoust, T.-R. Chang et al., Observation of Fermi arc surface states in a topological metal, Science 347, 294 (2015).
- [6] P. Hosur, S. A. Parameswaran, and A. Vishwanath, Charge Transport in Weyl Semimetals, Phys. Rev. Lett. 108, 046602 (2012).
- [7] A. A. Burkov, Weyl Metals, Annu. Rev. Condens. Matter Phys. 9, 359 (2018).
- [8] S. L. Adler, Axial-Vector Vertex in Spinor Electrodynamics, Phys. Rev. 177, 2426 (1969).
- [9] J. S. Bell and R. Jackiw, A PCAC puzzle: $\pi^0 \gamma \gamma$ in the σ -model, Nuov. Cim. A **60**, 47 (1969).
- [10] H. B. Nielsen and M. Ninomiya, The Adler-Bell-Jackiw anomaly and Weyl fermions in a crystal, Phys. Lett. B **130**, 389 (1983).
- [11] L. Balents, Weyl electrons kiss, Physics (College. Park. MD). 4, 36 (2011).
- [12] J. Liu, F. Xia, D. Xiao, F. J. García de Abajo, and D. Sun, Semimetals for high-performance photodetection, Nat. Mater. 19, 830 (2020).
- [13] M.-X. Guan, E. Wang, P.-W. You, J.-T. Sun, and S. Meng, Manipulating Weyl quasiparticles by orbital-selective photoexcitation in WTe2, Nat. Commun. 12, 1885 (2021).
- [14] N. P. Armitage, E. J. Mele, and A. Vishwanath, Weyl and Dirac semimetals in three dimensional solids, Rev. Mod. Phys. 90, 015001 (2018).
- [15] K. Taguchi, T. Imaeda, M. Sato, and Y. Tanaka, Photovoltaic chiral magnetic effect in Weyl semimetals, Phys. Rev. B 93, 201202(R) (2016).
- [16] T. Morimoto, S. Zhong, J. Orenstein, and J. E. Moore, Semiclassical theory of nonlinear magneto-optical responses with applications to topological Dirac/Weyl semimetals, Phys. Rev. B 94, 245121 (2016).
- [17] C.-K. Chan, N. H. Lindner, G. Refael, and P. A. Lee, Photocurrents in Weyl semimetals, Phys. Rev. B 95, 041104(R) (2017).
- [18] E. J. König, H.-Y. Xie, D. A. Pesin, and A. Levchenko, Photogalvanic effect in Weyl semimetals, Phys. Rev. B 96, 075123 (2017).
- [19] L. E. Golub, E. L. Ivchenko, and B. Z. Spivak, Photocurrent in gyrotropic Weyl semimetals, JETP Lett. 105, 782 (2017).
- [20] K. Sun, S.-S. Sun, L.-L. Wei, C. Guo, H.-F. Tian, G.-F. Chen, H.-X. Yang, and J.-Q. Li, Circular Photogalvanic Effect in the Weyl Semimetal TaAs, Chin. Phys. Lett. 34, 117203 (2017).
- [21] Q. Ma, S.-Y. Xu, C.-K. Chan, C.-L. Zhang, G. Chang, Y. Lin, W. Xie, T. Palacios, H. Lin, S. Jia *et al.*, Direct optical detection of Weyl fermion chirality in a topological semimetal, Nat. Phys. 13, 842 (2017).
- [22] Y. Zhang, H. Ishizuka, J. van den Brink, C. Felser, B. Yan, and N. Nagaosa, Photogalvanic effect in Weyl semimetals from first principles, Phys. Rev. B 97, 241118(R) (2018).

- [23] J. Ahn, G.-Y. Guo, and N. Nagaosa, Low-Frequency Divergence and Quantum Geometry of the Bulk Photovoltaic Effect in Topological Semimetals, Phys. Rev. X 10, 041041 (2020).
- [24] H. Watanabe and Y. Yanase, Chiral Photocurrent in Parity-Violating Magnet and Enhanced Response in Topological Antiferromagnet, Phys. Rev. X 11, 011001 (2021).
- [25] V. I. Belinicher and B. I. Sturman, The photogalvanic effect in media lacking a center of symmetry, Sov. Phys. Usp. **23**, 199 (1980).
- [26] E. Ivchenko and G. Pikus, Superlattices and Other Heterostructures: Symmetry and Optical Phenomena, Springer Series in Solid-State Sciences (Springer, Berlin, 2012)
- [27] J. E. Sipe and A. I. Shkrebtii, Second-order optical response in semiconductors, Phys. Rev. B 61, 5337 (2000).
- [28] F. de Juan, A. G. Grushin, T. Morimoto, and J. E. Moore, Quantized circular photogalvanic effect in Weyl semimetals, Nat. Commun. 8, 15995 (2017).
- [29] D. Rees, K. Manna, B. Lu, T. Morimoto, H. Borrmann, C. Felser, J. Moore, D. H. Torchinsky, and J. Orenstein, Helicity-dependent photocurrents in the chiral Weyl semimetal RhSi, Sci. Adv. 6, eaba0509 (2020).
- [30] G. B. Osterhoudt, L. K. Diebel, M. J. Gray, X. Yang, J. Stanco, X. Huang, B. Shen, N. Ni, P. J. W. Moll, Y. Ran, and K. S. Burch, Colossal mid-infrared bulk photovoltaic effect in a type-I Weyl semimetal, Nat. Mater. 18, 471 (2019).
- [31] Y. Zhang, T. Holder, H. Ishizuka, F. de Juan, N. Nagaosa, C. Felser, and B. Yan, Switchable magnetic bulk photovoltaic effect in the two-dimensional magnet CrI3, Nat. Commun. 10, 3783 (2019).
- [32] T. Holder, D. Kaplan, and B. Yan, Consequences of time-reversal-symmetry breaking in the light-matter interaction: Berry curvature, quantum metric, and diabatic motion, Phys. Rev. Research 2, 033100 (2020).
- [33] R. Fei, W. Song, and L. Yang, Giant photogalvanic effect and second-harmonic generation in magnetic axion insulators, Phys. Rev. B 102, 035440 (2020).
- [34] V. L. Alperovich, V. I. Belinicher, V. N. Novikov, and A. S. Terekhov, Surface photogalvanic effect in solids—Theory and experiment for band-to-band transitions in gallium arsenide, Zh. Eksp. Teor. Fiz. 80, 2298 (1981) [Sov. Phys. JETP 53, 1201 (1981)].
- [35] L. I. Magarill and M. V. Ehntin, Surface photogalvanic effect in metals, Zh. Eksp. Teor. Fiz. 81, 1001 (1981) [Sov. Phys. JETP 54, 531 (1981)].
- [36] J. E. Moore and J. Orenstein, Confinement-Induced Berry Phase and Helicity-Dependent Photocurrents, Phys. Rev. Lett. 105, 026805 (2010).
- [37] P. Hosur, Circular photogalvanic effect on topological insulator surfaces: Berry-curvature-dependent response, Phys. Rev. B 83, 035309 (2011).
- [38] A. Junck, G. Refael, and F. von Oppen, Photocurrent response of topological insulator surface states, Phys. Rev. B 88, 075144 (2013).
- [39] N. H. Lindner, A. Farrell, E. Lustig, G. Refael, and F. von Oppen, Lighting up topological insulators: Large surface photocurrents from magnetic superlattices, arXiv:1403.0010
- [40] K. W. Kim, T. Morimoto, and N. Nagaosa, Shift charge and spin photocurrents in dirac surface states of topological insulator, Phys. Rev. B 95, 035134 (2017).

- [41] Q. Wang, J. Zheng, Y. He, J. Cao, X. Liu, M. Wang, J. Ma, J. Lai, H. Lu, S. Jia *et al.*, Robust edge photocurrent response on layered type II Weyl semimetal WTe2, Nat. Commun. 10, 5736 (2019).
- [42] G. Chang, J.-X. Yin, T. Neupert, D. S. Sanchez, I. Belopolski, S. S. Zhang, T. A. Cochran, Z. Chéng, M.-C. Hsu, S.-M. Huang, B. Lian, S.-Y. Xu, H. Lin, and M. Z. Hasan, Unconventional Photocurrents from Surface Fermi Arcs in Topological Chiral Semimetals, Phys. Rev. Lett. 124, 166404 (2020).
- [43] F. D. M. Haldane, Attachment of surface "Fermi arcs" to the bulk Fermi surface: "Fermi-level plumbing" in topological metals, arXiv:1401.0529.
- [44] A. A. Burkov, Anomalous Hall Effect in Weyl Metals, Phys. Rev. Lett. 113, 187202 (2014).
- [45] P. J. W. Moll, N. L. Nair, T. Helm, A. C. Potter, I. Kimchi, A. Vishwanath, and J. G. Analytis, Transport evidence for Fermi-arc-mediated chirality transfer in the Dirac semimetal Cd₃As₂, Nature (London) 535, 266 (2016).
- [46] C. M. Wang, H. P. Sun, H. Z. Lu, and X. C. Xie, 3D Quantum Hall Effect of Fermi Arc in Topological Semimetals, Phys. Rev. Lett. 119, 136806 (2017).
- [47] J. Behrends, R. Ilan, and J. H. Bardarson, Anomalous conductance scaling in strained Weyl semimetals, Phys. Rev. Research 1, 032028(R) (2019).
- [48] C. Zhang, Z. Ni, J. Zhang, X. Yuan, Y. Liu, Y. Zou, Z. Liao, Y. Du, A. Narayan, H. Zhang *et al.*, Ultrahigh conductivity in Weyl semimetal NbAs nanobelts, Nat. Mater. 18, 482 (2019).
- [49] P. O. Sukhachov, M. V. Rakov, O. M. Teslyk, and E. V. Gorbar, Fermi arcs and DC transport in nanowires of Dirac and Weyl semimetals, Ann. Phys. 532, 1900449 (2020).
- [50] M. Breitkreiz and P. W. Brouwer, Large Contribution of Fermi Arcs to the Conductivity of Topological Metals, Phys. Rev. Lett. **123**, 066804 (2019).
- [51] V. Kaladzhyan and J. H. Bardarson, Quantized Fermi-arc-mediated transport in Weyl semimetal nanowires, Phys. Rev. B 100, 085424 (2019).
- [52] C. Zhang, Y. Zhang, H.-Z. Lu, X. C. Xie, and F. Xiu, Cycling Fermi arc electrons with Weyl orbits, Nat. Rev. Phys. 3, 660 (2021).
- [53] M. Breitkreiz, Parabolic Hall effect due to Co-Propagating Surface Modes, Phys. Rev. Research 2, 012071(R) (2020).
- [54] P. M. Perez-Piskunow, N. Bovenzi, A. R. Akhmerov, and M. Breitkreiz, Chiral anomaly trapped in Weyl metals: Nonequilibrium valley polarization at zero magnetic field, SciPost Phys. 11, 046 (2021).
- [55] N. Morali, R. Batabyal, P. K. Nag, E. Liu, Q. Xu, Y. Sun, B. Yan, C. Felser, N. Avraham, and H. Beidenkopf, Fermi-arc diversity on surface terminations of the magnetic Weyl semimetal Co3Sn2S2, Science 365, 1286 (2019).
- [56] J. Fujii, B. Ghosh, I. Vobornik, A. B. Sarkar, D. Mondal, C.-N. Kuo, F. C. Bocquet, L. Zhang, D. W. Boukhvalov, C. S. Lue, A. Agarwal, and A. Politano, Mitrofanovite Pt₃Te₄: A topological metal with termination-dependent surface band structure and strong spin polarization, ACS Nano 15, 14786 (2021).

- [57] S. Li and A. V. Andreev, Spiraling Fermi arcs in Weyl materials, Phys. Rev. B 92, 201107(R) (2015).
- [58] Arc-arc transitions may play a role in some special situations. For instance, large Chern numbers |C| > 1 imply the presence of several arc sheets and thus energy and momentum conserving arc-arc transitions become a possibility. Similarly, unscreened surface potentials may lead to strongly dispersing Fermi arcs [57], which may in principle enable intra-arc transitions. We preclude these issues by assuming $C = \pm 1$ and linear arc dispersion.
- [59] E. Liu, Y. Sun, N. Kumar, L. Muechler, A. Sun, L. Jiao, S.-Y. Yang, D. Liu, A. Liang, Q. Xu *et al.*, Giant anomalous Hall effect in a ferromagnetic kagome-lattice semimetal, Nat. Phys. 14, 1125 (2018).
- [60] T. Suzuki, R. Chisnell, A. Devarakonda, Y.-T. Liu, W. Feng, D. Xiao, J. Lynn, and J. Checkelsky, Large anomalous Hall effect in a half-Heusler antiferromagnet, Nat. Phys. 12, 1119 (2016).
- [61] M. V. Berry and R. J. Mondragon, Neutrino billiards: Timereversal symmetry-breaking without magnetic fields, Proc. R. Soc. London A 412, 53 (1987).
- [62] N. Bovenzi, M. Breitkreiz, T. E. O'Brien, J. Tworzydło, and C. W. J. Beenakker, Twisted Fermi surface of a thin-film Weyl semimetal, New J. Phys. 20, 023023 (2018).
- [63] J. F. Steiner, A. V. Andreev, and D. A. Pesin, Anomalous Hall Effect in Type-I Weyl Metals, Phys. Rev. Lett. 119, 036601 (2017).
- [64] A. Avdoshkin, V. Kozii, and J. E. Moore, Interactions Remove the Quantization of the Chiral Photocurrent at Weyl Points, Phys. Rev. Lett. 124, 196603 (2020).
- [65] Here we neglect one length scale of the problem, which is the mean free path τv given by the relaxation time τ . Within the semiclassical approach described in Sec. II C the mean free path is assumed long compared to essentially all other relevant scales, which makes the mean free path itself irrelevant for the following discussion.
- [66] P. J. Moll, Focused ion beam microstructuring of quantum matter, Annu. Rev. Condens. Matter Phys. **9**, 147 (2018).
- [67] S. Nishihaya, M. Uchida, Y. Nakazawa, R. Kurihara, K. Akiba, M. Kriener, A. Miyake, Y. Taguchi, M. Tokunaga, and M. Kawasaki, Quantized surface transport in topological Dirac semimetal films, Nat. Commun. 10, 2564 (2019).
- [68] A. Bedoya-Pinto, A. K. Pandeya, D. Liu, H. Deniz, K. Chang, H. Tan, H. Han, J. Jena, I. Kostanovskiy, and S. S. Parkin, Realization of epitaxial NbP and TaP Weyl semimetal thin films, ACS Nano 14, 4405 (2020).
- [69] P. Qin, Z. Feng, X. Zhou, H. Guo, J. Wang, H. Yan, X. Wang, H. Chen, X. Zhang, H. Wu et al., Anomalous Hall effect, robust negative magnetoresistance, and memory devices based on a noncollinear antiferromagnetic metal, ACS Nano 14, 6242 (2020).
- [70] J. Cao, M. Wang, Z.-M. Yu, and Y. Yao, Bulk-Fermi-arc transition induced large photogalvanic effect in Weyl semimetals, arXiv:2108.08138.